

12-15-2006

Optical Spectroscopy to Determine Intermediate Combustion Product Radicals in a Hydrocarbon Fueled Rocket Engine Exhaust Plume

Lester A. Langford
University of New Orleans

Follow this and additional works at: <https://scholarworks.uno.edu/td>

Recommended Citation

Langford, Lester A., "Optical Spectroscopy to Determine Intermediate Combustion Product Radicals in a Hydrocarbon Fueled Rocket Engine Exhaust Plume" (2006). *University of New Orleans Theses and Dissertations*. 493.

<https://scholarworks.uno.edu/td/493>

This Thesis is protected by copyright and/or related rights. It has been brought to you by ScholarWorks@UNO with permission from the rights-holder(s). You are free to use this Thesis in any way that is permitted by the copyright and related rights legislation that applies to your use. For other uses you need to obtain permission from the rights-holder(s) directly, unless additional rights are indicated by a Creative Commons license in the record and/or on the work itself.

This Thesis has been accepted for inclusion in University of New Orleans Theses and Dissertations by an authorized administrator of ScholarWorks@UNO. For more information, please contact scholarworks@uno.edu.

Optical Spectroscopy to Determine Intermediate
Combustion Product Radicals in a
Hydrocarbon Fueled Rocket Engine Exhaust Plume

A Thesis

Submitted to the Graduate Faculty of the
University of New Orleans
In Partial Fulfillment of the
Requirements for the Degree of

Master of Science
In
Engineering,
Electrical Engineering

By

Lester A. Langford

B.S. University of New Orleans, 2003

December, 2006

© 2006, Lester Langford

Dedication

To my wife, Megan , and my daughter, Katherin,
Thanks for putting up with me over the years while I finished....

Acknowledgment

After all those years, I've got quite a list of people who contributed in some way to this thesis, for which I would like to express thanks.

Kim Jovanovich, for guiding me with deft and subtle aim

Dr. Daniel Allgood, for the help with CFD and the detailed critique of how and what I was trying to do

Dr. Gopal Tejwani, for insight into the mysteries of the physics and kinetic chemistry of combustion physics

Jonathan Morris, for assistance and ridicule in Matlab and plotting complex data

Dr. W. W. (Bill) St. Cyr, for allowing me to undertake this study

Breanne Guillot and W. Mark Mitchell, without your efforts in acquiring quality data the analysis would not have been possible

Ruby Menge and everyone else in Bldg 8306, putting up with me at times had to have been trying

FSM, for guidance

To Katherin, my daughter, for all the nights dad came home late from school and all of the things we missed doing together,,,,, that part's done

And finally and most importantly,

Megan, my wife, for the love and support through the years, for the understanding, and for getting me moving in the mornings after so many late nights studying, thanks

Table of Contents:

List of Figures:	v
List of Tables:	vii
Abstract	viii
INTRODUCTION.....	1
THEORY	7
Characteristics of Rocket Exhaust Plumes.....	7
Radiation Processes.....	9
Non-isothermal Emission	11
Band Systems.....	13
EXPERIMENTAL	15
Methane Thruster Test Program.....	15
Spectroscopic Instrumentation	17
High-Resolution OMA1 System.....	19
Broadband OMA2 System	21
High-Resolution SPEC 10 System	22
Spectral System Calibration and Data Reduction	24
RESULTS	26
CEA Analysis.....	27
CFD Analysis.....	38
Experimental Results	43
CONCLUSIONS	57
REFERENCES.....	58
APPENDIX A – METHANE THRUSTER TESTBED P&ID.....	60
APPENDIX B - CEA O/F INPUT FILES:	61
APPENDIX C – SELECTED ENGINE TEST PROPELLANT FLOWRATES	62
APPENDIX D – CEA OUTPUT RESULTS	64
VITA.....	74

List of Figures:

FIGURE 1. TYPICAL UNDEREXPANDED PLUME STRUCTURE FOR AN INVISCID, NON- REACTING CORE SURROUNDED BY A VICOUS MANTLE. ¹⁰	8
FIGURE 2. ENERGY LEVELS AND TRANSITIONS IN A HYPOTHETICAL MOLECULE. ¹⁰	10
FIGURE 3. MTTP ROCKET SHOWING CHAMBER DIMENSIONS	16
FIGURE 4. TYPICAL SPECTRAL INSTRUMENTATION SETUP	19
FIGURE 5. C ₂ MOLE FRACTION AS A FUNCTION OF O/F RATIO AND CHAMBER PRESSURE	30
FIGURE 6. CH MOLE FRACTION AS A FUNCTION OF O/F RATIO AND CHAMBER PRESSURE	30
FIGURE 7. CN MOLE FRACTION AS A FUNCTION OF O/F RATIO AND CHAMBER PRESSURE	31
FIGURE 8. C MOLE FRACTION AS A FUNCTION OF O/F RATIO AND CHAMBER PRESSURE	31
FIGURE 9. CO MOLE FRACTION AS A FUNCTION OF O/F RATIO AND CHAMBER PRESSURE	32
FIGURE 10. TEMPERATURE AND CO MOLE FRACTION VS. O/F FOR A PC OF 150 PSIA	33
FIGURE 11. CO ₂ MOLE FRACTION AS A FUNCTION OF O/F RATIO AND CHAMBER PRESSURE	34
FIGURE 12. NO MOLE FRACTION AS A FUNCTION OF O/F RATIO AND CHAMBER PRESSURE	34
FIGURE 13. OH MOLE FRACTION AS A FUNCTION OF O/F RATIO AND CHAMBER PRESSURE	35
FIGURE 14. CHAMBER TEMPERATURE (°K) AS A FUNCTION OF O/F RATIO AND CHAMBER PRESSURE	36
FIGURE 15. VARIATION IN SPECIFIC IMPULSE WITH CHANGE IN O/F RATIO AND CHAMBER PRESSURE	38
FIGURE 16. PLUME GEOMETRY FOR CFD GRID GENERATION. ¹⁷	39
FIGURE 17. MTTP CFD TEMPERATURE PROFILE FOR O/F OF 1.8 AND PC OF 150 PSIA. BLACK LINE INDICATES THE LOS USED TO EXTRACT SPECIES CONCENTRATIONS. ¹⁷	41
FIGURE 18. EXTRACTED DATA SHOWING PLUME CO MASS FRACTION CONCENTRATION AND PLUME TEMPERATURE ALONG THE ANGLED LOS. ¹⁷	41
FIGURE 19. MTTP CFD TEMPERATURE PROFILE FOR O/F OF 1.8 AND PC OF 150 PSIA. BLACK LINE INDICATES THE LOS USED TO EXTRACT SPECIES CONCENTRATIONS ¹⁷	42
FIGURE 20. EXTRACTED DATA SHOWING PLUME CO MASS FRACTION CONCENTRATION AND PLUME TEMPERATURE ALONG THE PERPENDICULAR LOS. ¹⁷	42
FIGURE 21. SPECTRA VARIATION WITH CHANGE IN O/F RATIO, CONSTANT CHAMBER PRESSURE	45
FIGURE 22. SPECTRA VARIATION WITH CHANGE IN CHAMBER PRESSURE, CONSTANT O/F RATIO	47
FIGURE 23. SPECTRA VARIATION WITH CHANGE IN ENGINE OPERATING PARAMETERS	50

FIGURE 24. COLLECTION OPTIC CO-LINEAR CONFIGURATION FOR SPEC10 SYSTEM FOR TEST SERIES 21	53
FIGURE 25. COLLECTION OPTIC PERPENDICULAR CONFIGURATION FOR SPEC10 SYSTEM FOR TEST SERIES 22	53
FIGURE 25. SPECTRA VARIATION WITH CHANGE IN LOS	55

List of Tables:

TABLE 1. MOLECULAR BAND SYSTEM STRENGTH COMPARISON.....	46
TABLE 2. MOLECULAR BAND SYSTEM STRENGTH COMPARISON	48
TABLE 3.MOLECULAR BAND SYSTEM STRENGTH COMPARISON	51
TABLE 4. COLLECTION OPTIC ALIGNMENT ORIENTATION	52
TABLE 5. MOLECULAR BAND SYSTEM STRENGTH COMPARISON	56

Abstract

With the prospect of hydrocarbon-fueled rocket engines, such as Rocket Propellant 1 (RP-1) or methane (CH_4) fueled engines being considered for use in future space flight systems, the contributions of intermediate or final combustion products resulting from these hydrocarbon fuels are of great interest. The effect of several diatomic molecular radicals, such as Carbon Monoxide, Molecular Carbon, Methylene Radical, Cyanide or Cyano Radical, Hydroxyl, and Nitric Oxide, needs to be identified and the effects of their band systems on the spectral region from 300 nm to 850 nm determined. This work shows the effect of different engine operating parameters, oxidizer-to-fuel ratio and chamber pressure, and different optical alignments, different lines-of-sight and fields-of-view, on the spectral signature of the engine exhaust plume of a small hydrocarbon-fueled test engine. Computational results, along with experimental results of an extensive test program are presented.

Chapter 1

INTRODUCTION

IN October 1961, the site known today as NASA's John C. Stennis Space Center was selected to be the site of a static test facility for launch vehicles to be used in the Apollo manned lunar landing program. The site selected proved to be a practical and convenient one. The location was selected because of its water access, essential for transporting large rocket stages, components and loads of propellants. The largely undeveloped area offered a large swath of uninhabited land, which could provide the 13,500-acre test facility with a sound buffer of close to 125,000 acres.

The center's primary mission at the beginning was to certify for flight all of the first and second stages of the Saturn V rocket to be used for the Apollo program. On April 23, 1966, the first rocket engine static test-firing performed at the Stennis Space Center (SSC) was conducted on the A-2 Test Stand. That test was on the second stage of the Saturn V moon rocket which consisted of a cluster of five J-2 rocket engines. This program continued into the early 1970s. After the Apollo program ended, the flight certification testing of the Space Shuttle Main Engine (SSME) became the primary testing activity at SSC since June of 1975. All of the liquid rocket engines used to boost the Space Shuttle into low-Earth orbit are flight certified at SSC on the same stands used to test fire all first and second stages of the Saturn V in the Apollo and Skylab programs.

SSC has undergone a number of name changes. Its original name, Mississippi Test Operations, was changed to Mississippi Test Facility in 1965. In 1974, the facility was named the National Space Technology Laboratories reporting to NASA Headquarters in Washington, D.C. In May 1988, it was renamed the John C. Stennis Space Center in honor of U.S. Sen. John C. Stennis of Mississippi.

Early in the development cycle of testing the Space Shuttle Main Engine, it was noted that the exhaust plume of the engine underwent various visible changes immediately preceding an engine failure. Multicolor streaks were evident in the exhaust plume, which led researchers to conclude that metallic particles from engine components were being entrained in the propellant flow and subsequently burning in the plume. Researchers from the Arnold Engineering Development Center, in Tullahoma, Tennessee, were brought in to apply spectroscopic techniques to the plume in an attempt to identify the effluent materials. The field of rocket engine exhaust plume diagnostics for vehicle health management as applied to propulsion ground testing arose from that effort.

The intention of the plume diagnostics program is to enhance test operation efficiency and provide for safe cutoff of rocket engines prior to incipient failure. Exhaust Plume emission spectroscopy has emerged as a comprehensive non-intrusive sensing technology which can be applied to a wide variety of engine performance conditions with a high degree of sensitivity and specificity. Stennis Space Center researchers have been in the forefront of advancing experimental techniques and developing theoretical approaches in order to bring this technology to a more mature and fruitful stage. The current focus of

these efforts is the SSME. SSME exhaust plume spectral data have been routinely acquired at the SSC test stands since 1989 by utilizing an optical multi-channel analyzer (OMA)-based system.¹ The instrumentation used to acquire this spectroscopic information has matured over the years to the present day's capability of acquiring sub-nanometer resolution in the spectrum collected. Specific information on the engine components and any materials which can wear away, by normal means or as a result of an engine malfunction, and introduce matter into the exhaust plume is critical to any quantitative or qualitative interpretation of the plume spectral features and any correlation of those features as it may impact engine performance conditions. This information is compiled in the materials database, such as the SSME materials database.²

Engine health monitoring utilizing real-time optical spectroscopic techniques is a relatively young field. Instrumentation and monitoring technologies have been developed by SSC researchers to effectively assess high and low temperature rocket plume using atomic absorption and emission techniques. Various optical instruments, including high- and low-resolution Optical Multichannel Analyzer (OMA) based systems and the high-speed polychromator system (HSPCS)¹, have been continuously used to acquire SSME exhaust plume spectral emission data on the sea level test stands.

The development of new analytical tools and techniques completed by SSC in 1994^{3,4} began the technique's application and validation process. These developments jumpstarted plume diagnostics from a mainly qualitative tool to a more insightful and powerful tool. The analytical tools developed are a line-by-line (LBL) spectral simulation

computer program³ and an automated post-test data analysis and expert system called Engine Diagnostics Console (EDC).⁴ Various engine testing and development activities such as alternate turbopump development (ATD) for high pressure fuel turbopump (HPFTP) and high pressure oxidizer turbopump (HPOTP)⁵ have benefited from the application of Plume Diagnostics techniques. Plume diagnostics was also applied to the simulated altitude test stand in 1997, using atomic absorption instrumentation developed at SSC.⁶ Plume diagnostics methods successfully detected problems with one or more components before traditional sensors on several occasions. Some of the benefits of applying plume diagnostics techniques to engine testing are : extending the time between expensive inspections, predicting bearing wear, providing an accurate timeline for failure analysis and a verification tool for determining required engine design modifications. Providing these capabilities requires the accurate identification and quantification of all effluent material(s) in the plume.

During a SSME engine test, atomic emissions from 10 elements, which are strongly to moderately emitting and which are constituents of the major alloys utilized in the SSME, are monitored to help determine the overall health of the engine.⁷ The elemental contributions in the plume are measured and quantified. The elements monitored are: Ni, Fe, Cr, Co, Mn, Cu, Ag, Al, Ca, and Pd. The primary atomic emission lines of these elements are monitored using a high resolution spectral system covering the spectral region of 320 to 429 nm. A low-resolution, broadband spectral system is used to monitor the oxides, hydrides, and hydroxides of the 10 elements of interest in the spectral region of 300 to 850 nm, along with the oxides of Ti and Y. The SSME plume is dominated by OH and H₂O spectral bands as a result of clean burning liquid hydrogen fuel with liquid

oxygen oxidizer. Analytical techniques for removing the contributions of the OH and H₂O spectra have been developed and since their primary emission regions are outside of 320 nm to 850 nm, the interference is minimal.

Recently, the President committed the United States (2004) to a long-term human and robotic program to explore the solar system, starting with a return to the Moon that will ultimately enable future exploration of Mars and other destinations. The new spacecraft, the Crew Exploration Vehicle, will be developed and start testing by 2008 and will conduct its first manned mission no later than 2014. The Crew Exploration Vehicle will also be capable of transporting astronauts and scientists to the International Space Station after the Shuttle is retired. Presently, research is ongoing to determine the most advantageous fuel to use for the upper stage engines. Extensive efforts are being devoted to the study of hydrocarbon fuels, i.e. kerosene, methane, jet fuel, etc. These propellants are generally easier and safer to handle than liquid hydrogen, and are expected to bring down the costs associated with propellant transport and storage, and in spacecraft development and on-ground operations.

For hydrocarbon-fueled engines, such as RP-1 or CH₄ fueled engines, the plume is different due to the presence of several other species such as CO₂, C₂, CO, CH, CN, and NO in the plume, along with H₂O and OH. These species occur as intermediate or final combustion products or as a result of mixing of the hot plume with the atmosphere.

In order to extend the full capabilities of Plume Diagnostics to the hydrocarbon-fueled engine arena, an understanding of the plume spectral contributions of these species was undertaken. The capabilities of the SSC rocket plume spectroscopy simulation code (RPSSC) was extended by incorporating the latest and most accurate molecular and spectroscopic parameters for C_2 , CO, CH, CN, and NO.^{8,9} All the relevant bands for these five molecules were included in the program. A testing program utilizing a gaseous methane/gaseous oxygen fueled thruster was implemented, with the express purpose of identifying intermediate combustion product radicals in a hydrocarbon fueled rocket engine exhaust plume. It is necessary to determine if the spectral bands associated with the species identified have any effect on the wavelength regions monitored for the metallic effluents associated with engine health monitoring.

In this work, the identification of the spectral bands attributed to CO_2 , C_2 , CO, CH, CN, OH, and NO in the plume and how the contributions of the selected species intensity profiles changed the monitored spectrum due to the change in the oxidizer-to-fuel (O/F) ratio was investigated. Different lines-of-sight and fields-of-view were also utilized in an attempt to determine the optimum configuration for the spectral data acquisition system.

Chapter 2

THEORY

The theoretical basis of plume emission spectroscopic techniques will be presented in order to relate the computational model obtained to the actual experimental results. The structure of the typical rocket exhaust plume resulting from a conical nozzle will be presented to validate the choice of the Mach diamond region as the target of choice for the spectral instrumentation. The general processes which give rise to the emission of radiation will be briefly discussed, and then the specific case of non-isothermal emission resulting from a rocket's exhaust plume will be reviewed. Finally, the band systems produced by the relevant hydrocarbon radicals of interest will be examined in general detail.

Characteristics of Rocket Exhaust Plumes

A rocket exhaust plume is formed by the rapid expansion of high-temperature, high-pressure products of chemical reactions in the engine combustion chamber to supersonic velocities at the exit of the nozzle. These high velocity products are at a much lower temperature than the low velocity products in the chamber due to the thrust producing conversion of thermal to kinetic energy in the expansion. The resultant plume can be characterized as consisting of two distinct components: a more or less inviscid, non-

reacting core surrounded by a viscous mantle in which reactions are taking place by mixing with the ambient atmosphere. Fig. 1 shows the structure of a typical underexpanded plume.¹⁰

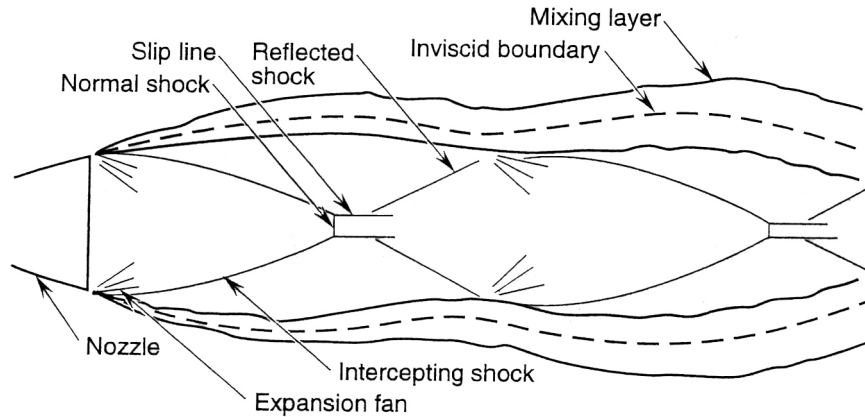


FIGURE 1. TYPICAL UNDEREXPANDED PLUME STRUCTURE FOR AN INVISCID, NON-REACTING CORE SURROUNDED BY A VICOUS MANTLE.¹⁰

The structure of the core underexpanded exhaust flow of an engine producing only gaseous products will expand to a pressure slightly above that of the local atmospheric pressure. The gas flow will expand until the dynamic pressure of the external flow forces it to reflect. As a supersonic flow, it can only do so through an oblique shock wave. This reflected shock will propagate to the centerline of the plume where it will be reflected again. The plume gases flowing through these shock waves become compressed to a pressure above the external value. This process repeats itself to form a pattern of Mach diamonds. The resultant core flow is nearly parallel to the axis. At certain external pressures, the momentum and energy of the flow cannot remain conserved in an inviscid flow across an oblique shock as it approaches the plume axis. As a result, a normal shock

forms at the plume axis. The leading edge of the Mach diamond is called the Mach disc. Downstream of this disc, the flow is subsonic and higher temperature, approaching the stagnation temperature. This higher temperature region is required for the application of emission spectroscopic techniques.

As the exhaust jet boundary leaves the rocket nozzle, the velocity of the exhaust gases differs generally from that of the surrounding free stream. Here the real gas effects are encountered, specifically the viscosity, which introduces a turbulence which causes mixing of the exhaust and ambient gases that will propagate downstream to form the mixing layer of the plume. Several effects are occurring in this layer, momentum and energy are being exchanged, and chemical reactions are occurring between exhaust and atmospheric species.

Radiation Processes

Rocket exhaust plume emission is generally thermally driven, occurring from changes in the internal energy of the constituent molecules, the products of combustion. Those changes in the molecular energy levels are accompanied by the emission of radiation, provided certain quantum-mechanical conditions are met. A diagram of the emissive process is displayed in Fig. 2.¹⁰ The figure shows the variation of the energy level with the internuclear separation of a hypothetical molecule. In the lower part of the figure, as the molecule vibrates, there is a continual exchange of potential and kinetic energy. This is due to the excursions of the nuclei which increase with temperature until the

dissociation level is reached. When that level is reached, the nuclei fly apart. At absolute zero, the oscillations are minimal. In between, there are certain levels between which sudden jumps can occur as a consequence of the absorption or emission of a photon.

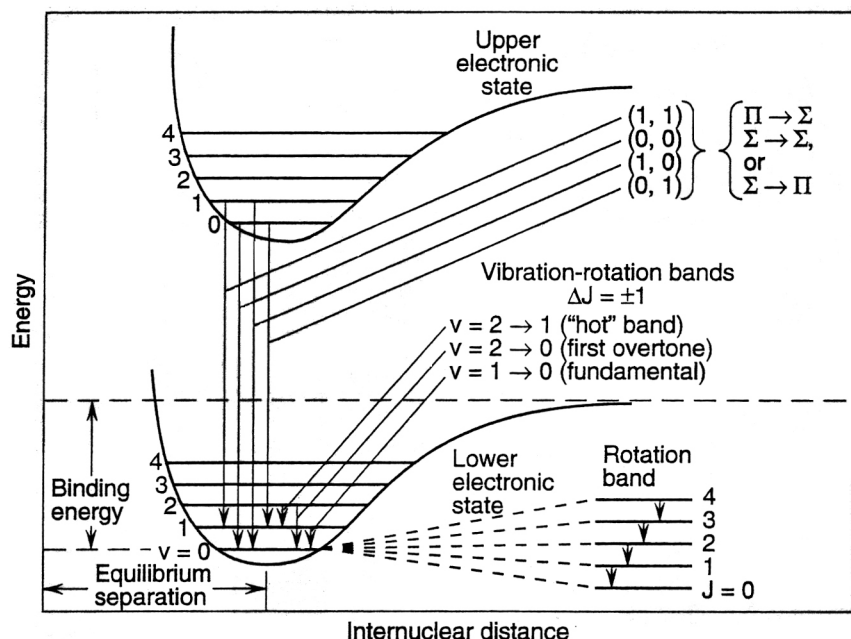


FIGURE 2. ENERGY LEVELS AND TRANSITIONS IN A HYPOTHETICAL MOLECULE.¹⁰

With such changes in the vibrational energy, there are changes in the rotational energy associated with the molecule. Each of the vibrational levels indicated in the figure has a substructure of rotational levels. Depending on the molecular composition, a simultaneous change in rotational level can either be allowed or is demanded by the *selection rules* of quantum mechanics. As a result, thermal emission from molecular gases appears in characteristic vibration-rotation bands, which are groupings of spectral lines, each of which can be associated with a particular transition from one level to another, identified in terms of the vibration and rotation quantum numbers, v and J . The

fundamental band is defined as that arising from a transition between the first excited level to the ground state; overtone bands involve transitions of two or more vibrational levels; and hot bands are those involving changes of energy levels not including the ground state.

Along with energy contained in vibrations and rotations, molecules can also possess internal energy in the electronic structure. A depiction of vibrational motion when the molecular structure is altered by a quantum of electronic energy is shown in the upper part of Fig. 2. A spontaneous transition from this state to the lower one would be associated with the emission of a photon. Close examination of the figure shows a hierarchy of three levels. The transitions from higher to lower electronic states involve the most energy. So, the electronic bands with their fine structure caused by associated changes in vibration and rotation appear in the ultraviolet and visible regions of the spectrum. Vibration bands lie in the near IR and the pure rotation bands at longer wavelengths. The band spectrum utilized for plume diagnostics engine health monitoring begins in the ultraviolet (~300nm), continue through the visible, and extend into the near IR (~850nm).

Non-isothermal Emission

The fundamental governing relation for the emission from a highly inhomogeneous non-isothermal source such as a rocket plume is the Schwarzschild *equation of radiative transfer*,¹⁰

$$-\frac{dI_v}{ds} = [j(v,s) - k(v,s)I_v(s)] \rho(s) \quad (2.1)$$

where the spectral radiance (specific intensity) I_v in a particular direction along a path s depends on the emission coefficient $j(v,s)$ and the absorption coefficient $k(v,s)$. Both of these are functions of the optical frequency v and the conditions, particularly the temperature, along the path, and the local density of emitting and absorbing species $\rho(s)$.

There is a special case of a non-scattering field in local thermodynamic equilibrium (LTE), such as a plume without particulate components to be considered. Local thermodynamic equilibrium in a gas dynamic system prevails when the rates of distribution of internal energy by collisions are very rapid compared to the rates of change in the gas temperature caused by expansion or compression in the flow, and to the radiative lifetimes of the emitting species. For this special case, the ratio of the emission and absorption coefficients is the Planck blackbody function. In this case, the equation for the integrated line radiance, defined as

$$I(T) = I_\lambda^*(T)W(T) \quad (2.2)$$

where I_λ is the spectral radiance and $I_\lambda^*(T)$ is the corresponding spectral radiance of a blackbody at the gas temperature, T , and $W(T)$ is the equivalent width of a spectral line, can be integrated to derive the form

$$I_{\nu} = \int_0^L k(\nu, s) \rho(s) I_{\nu}^*(T) e^{-\int_0^s k(\nu, s') \rho(s') ds'} ds \quad (2.3)$$

Where the quantity ahead of the exponential is the local emission attenuated by the absorption, as given by the exponential term, in traveling the remainder of the path to the boundary of the plume closer to the observer. The blackbody function, as well as the absorption coefficient, is a function of the local temperature, $T(s)$.

Band Systems

The molecular carbon, C_2 , band systems occur in virtually all hydrocarbon combustion processes. There are eight known C_2 band systems in the 2000 to 12000 nm spectral region.¹¹ Of these, the Swan band system, $d^3\Pi_g - a^3\Pi_u$ is the strongest.

The CH radical is a common intermediate in reactive chemical systems with hydrocarbons. The emission spectrum of the CH molecule in the visible and the near ultraviolet region contains three band systems, 4300 Å system ($A^2\Delta - X^2\Pi$), 3900 Å system ($B^2\Sigma^- - X^2\Pi$), and 3143 Å system ($C^2\Sigma^+ - X^2\Pi$).¹² Their intensities decrease in the order in which they are given, the 3143 Å system being the weakest. This system also happens to overlap a very strong OH band system at 3064 Å.

The CN free radical is a very important diatomic molecule that plays a significant role in many chemical reactions for any high-temperature gas containing detectable amounts of

C and N₂. The three lowest known electronic states of the CN radical are the $X^2\Sigma^+$ ground state and the $A^2\Pi$ and $B^2\Sigma^+$ excited states.¹³ CN is a particularly stable radical and its spectrum is dominant in many reactions. The Violet system ($B^2\Sigma^+ - X^2\Sigma^+$) is most easily observed. At 3000 K and 10 cm pathlength, it has significant emission in the spectral regions of 350.9 to 358.7 nm, 373.9 to 388.0 nm, and 406.1 to 421.1 nm.¹⁴ The strongest emission for CN Violet band system occurs in the spectral region of 380 to 388 nm.¹⁴

CO is an important and a major product of hydrocarbon combustion. The efficiency of hydrocarbon fuel-based combustion can be measured and quantified by monitoring the partitioning between an incomplete combustion product (CO) and the complete combustion product (CO₂). A small fraction of CO is expected to be in singly ionized state CO⁺ at typical plume temperatures giving rise to CO⁺ Comet-Tail band system. In cometary spectra, these bands are very common and are thought to arise through a resonance fluorescence excited by sunlight. For CO⁺ Comet-Tail band system, this band system has thousands of observable emission lines from 341.2 nm to 802.4 nm.¹⁴

The spectra of hydrogen flames always show the marked OH bands with band heads at 281 nm, 306 nm (strong), and 343 nm. The (0,0) band of the $A^2\Sigma - X^2\Pi$ OH band system is very strong with hundreds of strong emission lines in the spectral region of 300 to 320 nm and a few weaker lines, the (0,1) band, in the spectral region of 340 to 347 nm.^{15,16}

Chapter 3

EXPERIMENTAL

In order to study the plume reactants produced under typical rocket engine operating conditions, a unique experimental setup is required to generate a suitable exhaust plume. To meet these needs, the Methane Thruster Testbed Program was instituted at SSC. The test article, operating parameters and measurement instrumentation will be summarized.

Methane Thruster Test Program

The Methane Thruster Test Program (MTTP) testbed incorporates a 50 lb thrust Gaseous Oxygen/Gaseous Methane (GOX/GCH₄) thruster. The thruster originally designed for use with LOX/RP-1 propellants has been successfully used with methane. The thruster's chamber is radiatively cooled with a water-cooled nozzle. It is designed for flexibility and will operate at conditions well above those required for the study. The rocket chamber makes use of a modular design allowing the combustion chamber length to be modified as needs dictate. The chamber sections are held together by use of four threaded rods tightened onto flanges, creating a press-type configuration. The thruster design utilizes an L/D ratio of 4.35, an area ratio of the contracting portion of the nozzle of 20.199, and an area ratio of the expanding portion of the nozzle of 4.66.

The chamber is a heat-sink design made of oxygen-free high conductivity copper. The chamber circular cross-section is 50.8 mm (2 in.) in diameter from the injector face to the converging section of the nozzle. A shear coaxial injector introduces the propellants into the rocket chamber. The injector's oxygen post is recessed with respect to the injector face. The rocket is ignited by an independent, sparkplug fired igniter system that uses a separate chamber for gas mixing. GOX and Methane (CH_4) are injected off axis into the igniter's small combustion chamber to induce swirl to mix the two gas streams. The mixture is ignited by a spark plug driven by an oil furnace ignition transformer installed into an explosion-proof NEMA enclosure. Ignition is detected by a K-type thermocouple inserted into the igniter combustion chamber. The LabVIEW control software checks for a rise in temperature before the main propellant flow is introduced into the rocket chamber. The hot combustion gases flow into the rocket chamber and ignite the main propellant flow. Figure 3 shows a diagram of the MTTP rocket.

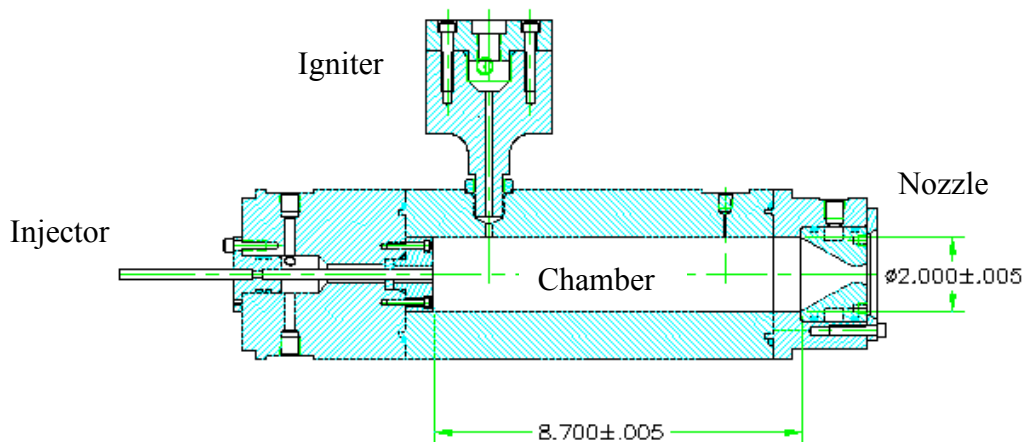


FIGURE 3. MTTP ROCKET SHOWING CHAMBER DIMENSIONS

The water-cooled nozzle assembly is also modular in design. Nozzles of different throat diameter can be interchanged, allowing the chamber pressure to vary for the same propellant flow rate. Also, different nozzle profiles can be used to vary the plume structure to optimize the shock structures produced. A Process and Instrumentation Diagram of the rocket test system is included in Appendix A.

Process instrumentation can be added at any point in the testbed. Current measurements include propellant pressures, mass flow rates and combustion chamber pressure and temperature. The MTTP system is controlled using National Instruments LabVIEW software operating SCXI based hardware. The National Instrument system handles all control functions as well as all engine and propellant delivery system data acquisition. The control system allows remote operation of the MTTP system.

Spectroscopic Instrumentation

Spectral measurements are performed using two optical multi-channel analyzer (OMA) systems, one high resolution and one broadband and eight video cameras. The high resolution OMA system (OMA1) is used to monitor the spectral region from 310 to 436 nm to cover the primary atomic emission lines of most of the significant metallics contained in alloys of interest. The broadband OMA system (OMA2) monitors the spectral region from 300 to 825 nm and is used primarily to cover the hydride, oxide, and hydroxide emissions of the elements of interest and the emission bands of the hydrocarbon fuels being tested. The two OMA systems have a temporal resolution of 0.5

s. The eight camera systems on the E-3 test stand provide visible, near IR and UV imaging of the exhaust plume and the engine systems. Due to hardware problems with the high resolution system (OMA1), a newer system (SPEC10) was deployed to acquire data on the plume. The switch was reluctant due to the large historical database that had been built up utilizing the older systems. The newer, improved spectral system does have several advantages due to advances in the design of the computer control and software, but it does have some drawbacks also.

Charge coupled devices (CCDs) can be roughly thought of as a two-dimensional grid of individual photodiodes (pixels), each connected to its own charge storage “well.” Each pixel senses the intensity of light falling on its collection area, and stores a proportional amount of charge in its associated “well.” Once charge accumulates for the specified exposure time (set in the software), the pixels are read out serially. CCD arrays perform three essential functions: photons are converted to electrons, integrated and stored, and finally read out. CCDs are very compact and rugged and can withstand direct exposure to relatively high light levels, magnetic fields, and RF radiation. They are easily cooled and can be precisely controlled to within a few tens of mille-degrees. A typical Spectral system is shown in Fig. 4.

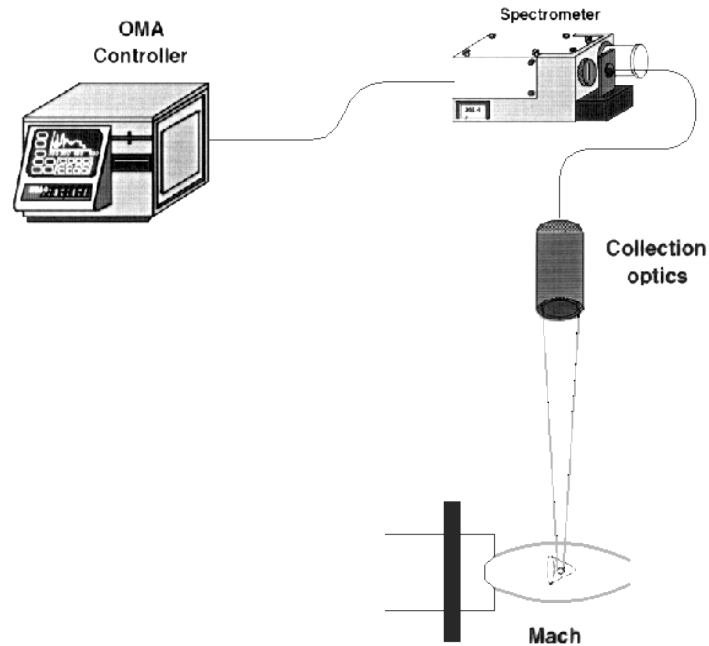


FIGURE 4. TYPICAL SPECTRAL INSTRUMENTATION SETUP

High-Resolution OMA1 System

The standard configuration for the OMA systems contains the following major hardware elements.

- Collection optics with two-inch diameter quartz lens with focal length of 2 in.
- Twenty-five meter, 200 micron diameter fused-silica fiber optic cable
- 0.32 meter Instruments SA[®] model HR-320 spectrometer
- 1024 element EG&G[®] model 1412 silicon photodiode detector
- EG&G[®] model 1460 OMA controller

The collection optics were positioned in several different positions to acquire data on the effect line-of-sight (LOS) had on the quality of the data gathered. The collection optics focuses the energy from the Mach diamond of the MTTP plume into the fiber optic cable, which transmits the energy to the spectrometer. Within the spectrometer, polychromatic light is separated into its monochromatic components, which are individually measured by the multi-element photodiode detector. The analog measurement signal of the detector is transmitted to the OMA, which controls the operation of the detector, digitizes the incoming data, and stores it to the internal system hard disk drive.

The spectrometer is a 0.32 m dispersive plane grating spectrometer in a Czerny-Turner configuration. In the 310-436 nm OMA system, the spectrometer uses a 600 grooves/mm plane reflection grating. Grating dispersion determines the spectral bandwidth and the dispersion and entrance slit width determines the spectral resolution. Higher grating dispersion results in higher resolutions, but the tradeoff is a reduced spectral window. The current configuration using a 600 grooves/mm grating with a 25 micron entrance slit, produces a spectral bandwidth about 126 nm wide, providing an average resolution of 0.123 nm per detector element.

The model 1412 detector is an un-intensified, thermo-electrically cooled, silicon photodiode array of 1024 individual detectors. Each detector array is 25 mm wide and 2.0 mm tall. The individual detector elements continuously integrate the incoming light from the exhaust plume throughout a programmed exposure time. At the end of an exposure, each detector element is read, its value passed to the OMA, and the next exposure begins.

Since the value from each detector element is digitized by a 14 bit A/D converter, the dynamic range of the detector is 16383 counts. A count level of 16383 indicates that the exposure was too long and the detector saturated. Experience shows that a 0.5 s exposure results in good signal levels while avoiding detector saturation.

The OMA digitizes the analog signals of the detector, buffers the resulting set of data points in its own RAM, and sets and resets the exposure timing sequence of the detector. It is configured with 6.5 Mbytes of RAM, and a 20 Mbyte hard drive. In addition, it is equipped with an IEEE-488 interface port, located on the I/O-A card of its backplane. The OMA is built around a standard VME bus that accepts a variety of VME bus plug-in cards. The I/O-A card is one such card that serves as an I/O interface and allows IEEE-488 devices to communicate with the OMA's CPU and access its RAM. The OMA uses about 4 Mbytes of RAM to buffer the data from a typical test firing.

Broadband OMA2 System

The system specifications used for the broadband optical system are the same as that for the High Resolution OMA1 system, except that the holographic grating has 147 grooves/mm. This gives a bandwidth of approximately 550 nm (300 – 850 nm). Every other specification is identical.

High-Resolution SPEC 10 System

The standard configuration for the SPEC 10 system contains the following major hardware elements.

- Collection optics with one-inch diameter quartz lens with focal length of 1 in.
- Twenty-five meter, 600 micron diameter fused-silica fiber optic cable
- 0.30 meter Acton SpectraPro 300i spectrometer
- Princeton Instruments Spec-10:100 1340 x 100 Back-illuminated imaging array
- Princeton Instruments® Model ST-138 CCD Camera Controller
- Computer running Windows 2000 or XP

The collection optic was again positioned in several different positions to try to determine the optimum position for best data acquisition.

The spectrometer is a 300-mm, f/4-aperture, triple-grating monochromator and spectrograph with dual exit ports, a large 14 x 27 mm focal plane, and an imaging optical system designed for multichannel CCD spectroscopy applications. The polished aspheric mirrors are used to achieve superior imaging with low scatter. The spectrometer has excellent spatial resolution. The triple-turret grating mount is populated with gratings of 300, 600, and 1200 grooves/mm, all with a 300 nm blaze angle. Setting the adjustable entrance slit to 20 microns, allowed for the best throughput to be achieved.

The Princeton Instruments Spec-10:100 1340 x 100 Back-illuminated imaging array is an un-intensified, thermo-electrically cooled, silicon photodiode array of 100 rows of 1340 individual detectors. The detector array is 26.8 mm wide and 2.0 mm tall. The individual detector elements are 20 x 20 μm in size. The exposure time is adjustable from 10 μs to multiple seconds. The dynamic range of the detector is 65,536 through a 16 bit A/D converter. A 0.1 s exposure time was utilized, resulting in good signal levels while avoiding detector saturation.

The detector is powered and controlled with a Princeton Instruments[®] Model ST-138 CCD Camera Controller. It offers dual A/D converters for optimized image collection at high speed or at high precision. The controller is connected to a computer through a high-speed serial link to DMA. The controller supports a variety of detectors and cameras and provides power and control for the thermoelectric cooling of the CCD detector. The controller has several useful features including: several built-in timing modes, on-chip charge binning control, readout mode options, readout time calculation, and array cleaning modes.

Princeton Instruments WinSpec is a 32-bit Windows[®] software package for digital imaging. WinSpec provides comprehensive image acquisition, display, processing, and archiving functions to allow complete data acquisition and analysis in one package. Spectrometer control and detector operation are independent functions under WinSpec, this allows the ability to collect data while simultaneously communicating with the spectrometer.

Spectral System Calibration and Data Reduction

Calibration of the spectral systems consists of two major parts: wavelength calibration and spectral radiance calibration. The calibration procedure begins with the wavelength calibration. The wavelength interval of each detector element in the CCD array is measured. A multi-element, hollow cathode lamp is used as the source for the spectral reference lines needed for the calibration. The lamp produces atomic emission lines for copper silver, nickel, iron, manganese, and chromium. These elements produce lines from approximately 324 nm to 550 nm. Since the wavelengths of these lines are precisely known, the wavelengths associated with several detector elements are assigned. The spectral system controller then performs a cubic fit to determine the wavelengths of the remaining detector elements. It should be noted that the calibration is as accurate as the spectral range per element. For the OMA spectral systems in high resolution configuration (600 groove/mm grating, 300–430 nm bandwidth), the wavelength calibration is accurate to within 0.123 nm. For the Spec10 system in a mid-band configuration (300 groove/mm, 300–560 nm bandwidth), the wavelength range is accurate to within 0.200 nm.

The systems are then calibrated for spectral radiance. An overfilled field of view (FOV) is used both during intensity calibration and during plume measurements. The lamp used is a NIST-traceable 1000 Watt FEL-M standard of spectral irradiance. The lamp is positioned on a portable optical rail precisely 30 cm from a 10 x 10 inch Lambertian screen. The spectral system's collection optic is positioned in the same plane as the lamp

filament, at a 15 degree angle. The collection optic views the radiance of the screen and the spectral system records the measured count level. Using the actual irradiance values of the lamp, provided by the lamp manufacturer, and the reflectance of the screen, the system generates a response function that relates a measured count level to an actual radiometric quantity at the wavelength of each detector element. The units of the response function are counts per radiance unit. The lamp-to-screen distance and the alignment of the system FOV in the center of the screen are the critical experimental factors for this type of calibration.

The spectral system converts the measured count level of a plume spectral scan to units of spectral radiance ($\text{W}/\text{cm}^2 \cdot \text{sr} \cdot \text{nm}$). Data is acquired from several seconds prior to engine ignition to several seconds after the engine has shut down. For the spectral intensity calibration, a scan without the lamp in operation is acquired for the purpose of subtracting out the light contribution to the signal from the ambient atmosphere. Also, thermal noise in the silicon detector array produces an offset level that adds to the plume signal. One of the spectral measurements taken immediately prior to the engine ignition is used as the background scan. This scan is taken to represent detector noise and ambient light effects. The background scan is subtracted from all subsequent spectral scans to isolate the contribution of the plume. Once the data have been corrected for background effects, it is converted to the correct radiometric units by applying the response function.

Chapter 4

RESULTS

To aid in identification of hydrocarbon combustion products in the plume which might also interfere with detection and quantification of metallic elements in the spectral region of 300 to 850 nm, plume monitoring utilizing plume diagnostics techniques was performed during hot-fire testing of the MTTP. The focus was on identifying, mainly carbon-based, combustion species emitting or absorbing in the spectral range from 300 to 850 nm. Through a literature search these species were found to be C₂, CO, and CH.^{8,9,14} Additionally; CN and NO have spectral bands in 300 to 850 nm, although neither was detected in the spectral data acquired. CN and NO molecules are not direct products of hydrocarbon-oxygen combustion systems unless nitrogen or a nitrogen compound is present as an impurity. However, these molecules can form in the boundary layer as a result of interaction of the hot plume with the atmosphere during the ground testing of engines. There are 10 electronic bands of these five molecules that needed to be identified and a determination made if they were present in the spectra acquired during testing. The ten additional band systems are: C₂ Swan, C₂ Phillips, CH 3900 Angstrom, CH 4300 Angstrom, CO Asundi, CO+ Comet-Tail, CN Violet, CN Red, NO Beta, and NO Gamma band systems.

In order to help determine the optimal LOS through the plume for the spectral systems, a Computational Fluid Dynamics simulation was run by Dr. D. Allgood.¹⁷ The model was

run on SSC's Beowulf computation cluster using CRUNCH CFD[®] software from Combustion Research and Flow Technology, Inc.^{18,19,20} The CRUNCH CFD[®] code package is a multi-element (*i.e.* tetrahedral, prismatic, pyramid, and hexahedral cells), unstructured flow solver for viscous, real gas systems for all flow regimes as well as multi-phase fluids. Its major features allow for generalized thermochemistry specifications, permits dynamic grid motion, and implementing a coupled two-equation turbulence model.

The input conditions for the CFD model were calculated using the Chemical Equilibrium with Applications (CEA) code developed at NASA's Glenn Research Center. CEA is a program which calculates chemical equilibrium product concentrations from any set of reactants and determines thermodynamic and transport properties for the product mixture. Built-in applications include calculation of theoretical rocket performance, Chapman-Jouguet detonation parameters, shock tube parameters, and combustion properties.

CEA Analysis

The static input parameters provided to the CRUNCH CFD code were obtained from the Chemical Equilibrium with Applications software package. The CEA equilibrium code of Gordon and McBride²¹ calculates the theoretical thermodynamic properties for an equilibrium mixture. The program can be applied to the design and analysis of equipment such as compressors, turbines, nozzles, engines, shock tubes, heat exchangers, and chemical processing equipment. The program can: calculate the chemical equilibrium

composition for assigned thermodynamic states; calculate theoretical rocket performance for a finite or infinite area combustion chamber; calculate Chapman-Jouguet detonations; or calculate shock tube parameters for both incident and reflected shocks.^{22,23}

To calculate the equilibrium composition of a rocket plume, the user is required to supply the state of the equilibrium mixture. The user provides the program with any two thermodynamic-state functions from the following list.

- (1) Temperature and pressure
- (2) Enthalpy and pressure
- (3) Entropy and pressure
- (4) Temperature and volume (or density)
- (5) Internal energy and volume (or density)
- (6) Entropy and volume (or density)

The shock and detonation problems require the use of input data of types (1) and (2).

Solving the rocket problem requires the input of data type (3) and type (1) or (2).

The thermodynamic data calculated by the program include conductivity, viscosity, species concentrations, specific heats, sound speed, equilibrium temperature and pressure, enthalpy, entropy, internal energy, and many others. The static pressure, temperature, (u,v,w) velocity components, and the mass fractions of the 13 species of

interest (CH_4 , CO , CO_2 , H , H_2 , H_2O , OH , O_2 , O , CH_3 , C_2H_2 , N_2 , $\text{C}_2(\text{s})$) are the parameters outputted by the CEA code which are needed for the input conditions to the CRUNCH CFD code.

A wide series of O/F's and chamber pressures were specified in the CEA input file to obtain the species concentrations for a range of conditions. The CEA input file parameters are specified in Appendix B.

The following plots demonstrate the effect of O/F and chamber pressure on the mole fraction of the species in the exhaust plume as calculated by CEA. The species concentration values are taken from the exit plane solutions output by the software. In Figs. 5 – 7, it can be noted that as the chamber pressure raises, the mole fraction of C_2 , CH and CN in the plume increases to a maximum at an O/F of 3.1, then decreases back to near zero at an O/F of 4.0. Since GOX/CH_4 combustion is stoichiometric at an O/F ratio of 4.0, combustion is theoretically complete at this ratio. The same curve shape is seen in Fig. 8, although the peak for the C curve is at an O/F ratio of 3.3. The difference in the peak location of C can be attributed to the higher plume temperature that occurs at the higher O/F, along with other more complex contributions. More investigation needs to be completed to verify all of the factors present which could play a part in this phenomenon.

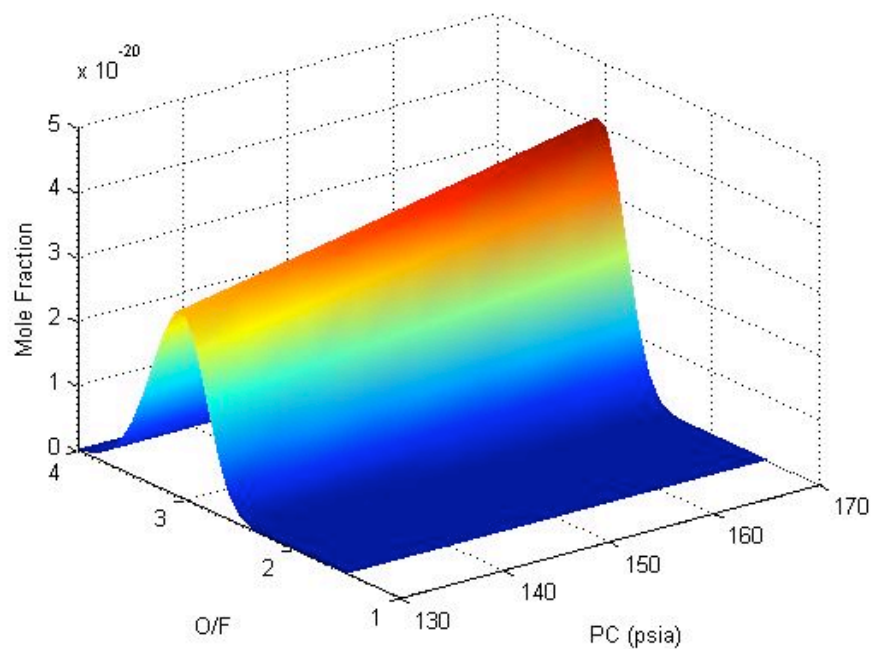


FIGURE 5. C_2 MOLE FRACTION AS A FUNCTION OF O/F RATIO AND CHAMBER PRESSURE

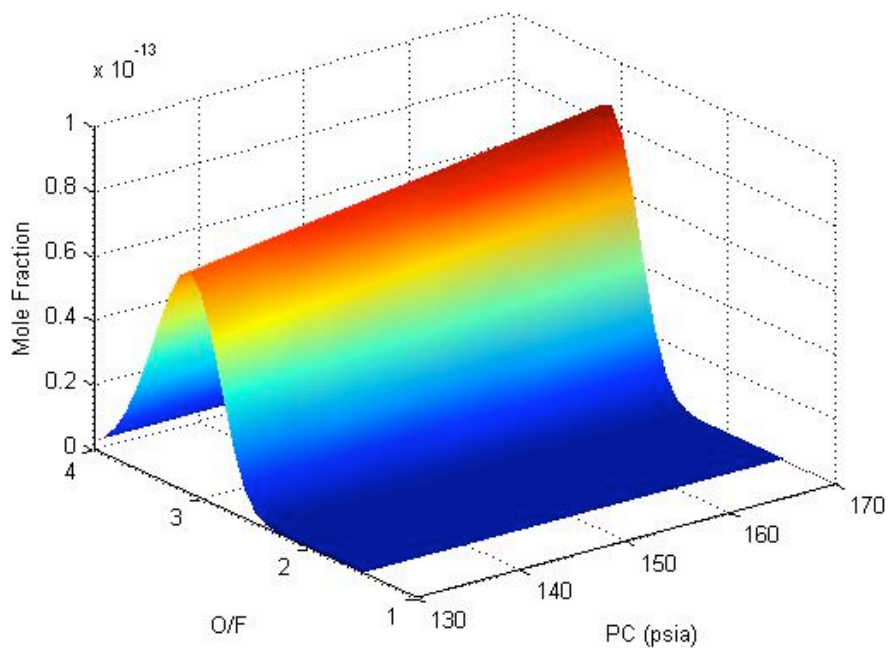


FIGURE 6. CH MOLE FRACTION AS A FUNCTION OF O/F RATIO AND CHAMBER PRESSURE

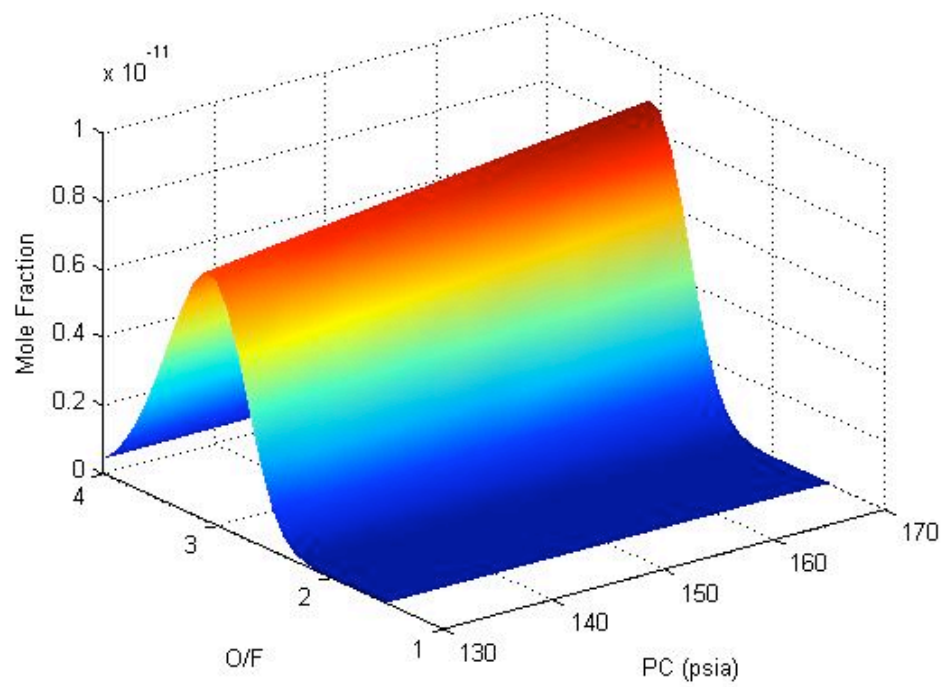


FIGURE 7. CN MOLE FRACTION AS A FUNCTION OF O/F RATIO AND CHAMBER PRESSURE

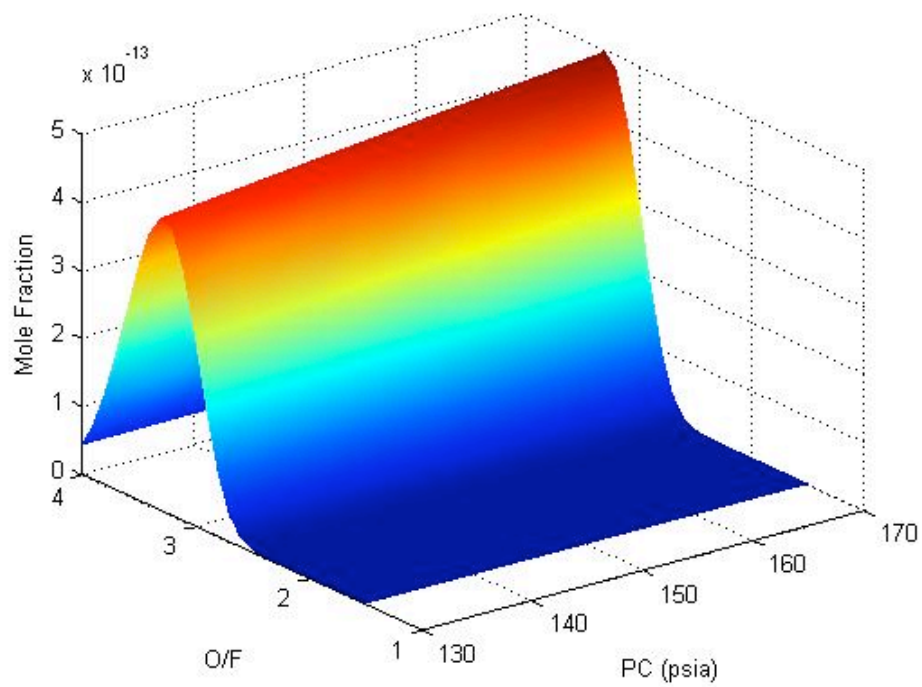


FIGURE 8. C MOLE FRACTION AS A FUNCTION OF O/F RATIO AND CHAMBER PRESSURE

The curve in Fig. 9 is the mole fraction concentration of CO as a factor of O/F and chamber pressure. The values peak at the fuel-rich portion (low O/F) of the graph showing that large quantities of CO are formed due to the lack of sufficient oxygen to complete the reaction to CO₂.²¹ The high levels of CO emissions at low O/F ratios are due to the slow rates of oxidation associated with low combustion temperatures. Increase in O/F ratio raises the flame temperature, which accelerates the rate of oxidation so that CO emissions decline. This phenomenon can be seen in Fig. 10.

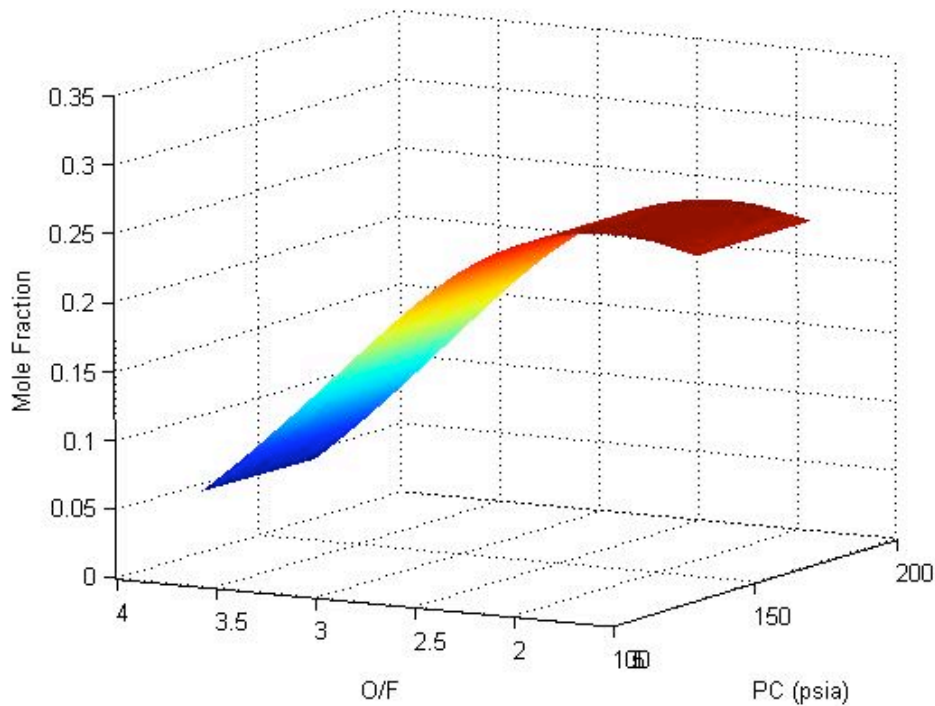


FIGURE 9. CO MOLE FRACTION AS A FUNCTION OF O/F RATIO AND CHAMBER PRESSURE

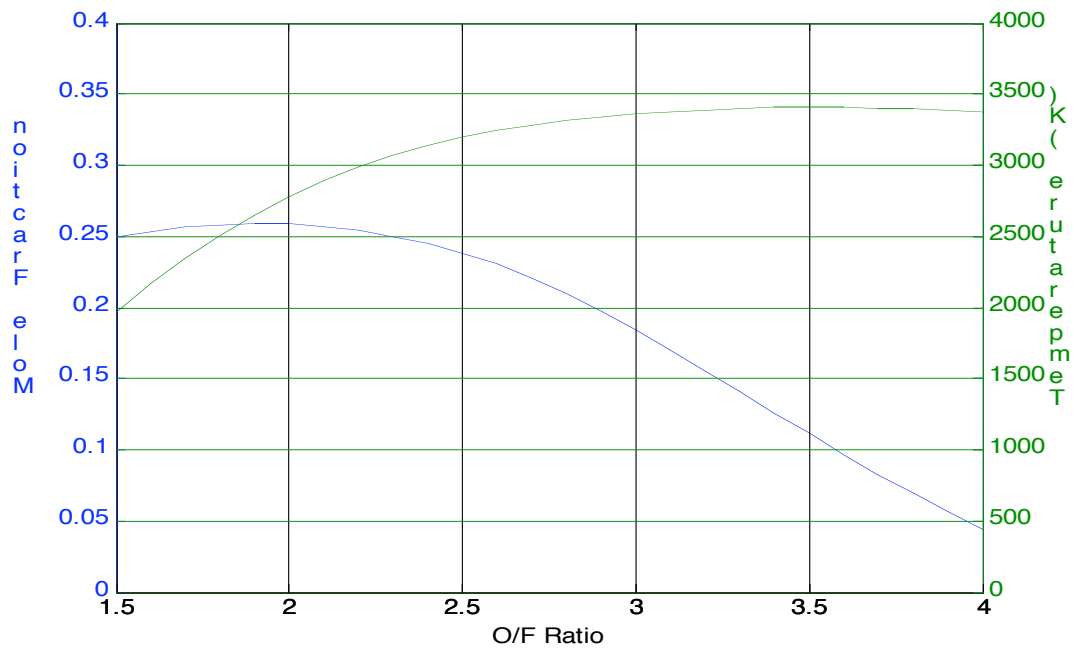


FIGURE 10. TEMPERATURE AND CO MOLE FRACTION VS. O/F FOR A PC OF 150 PSIA

Figures 11, 12, and 13 show the curves for CO_2 , NO, and OH, respectively, and all of these species show a marked increase with O/F ratio, indicating a strong dependence on plume temperature.

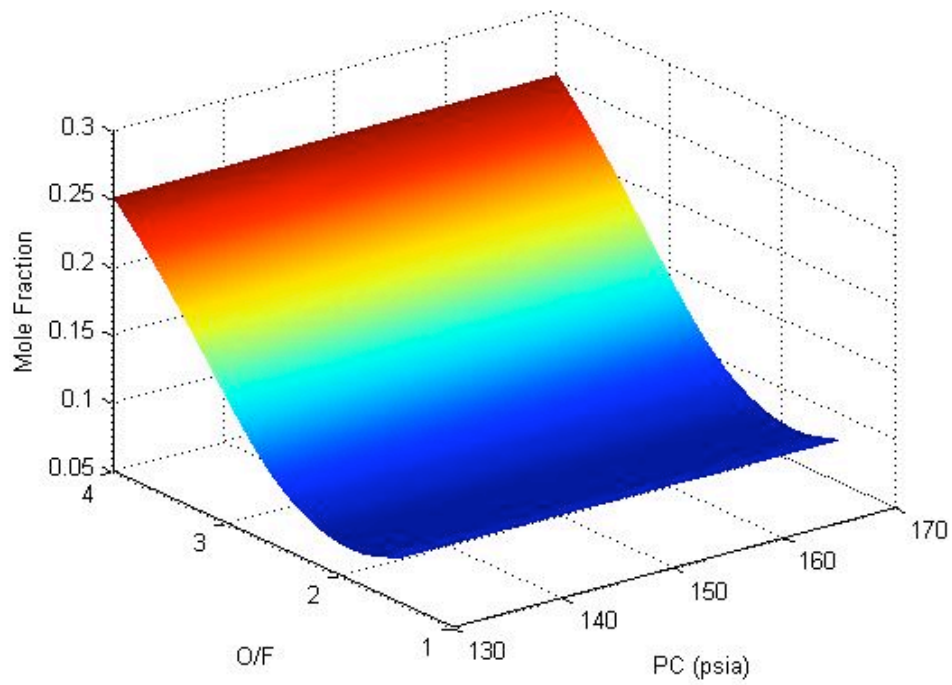


FIGURE 11. CO₂ MOLE FRACTION AS A FUNCTION OF O/F RATIO AND CHAMBER PRESSURE

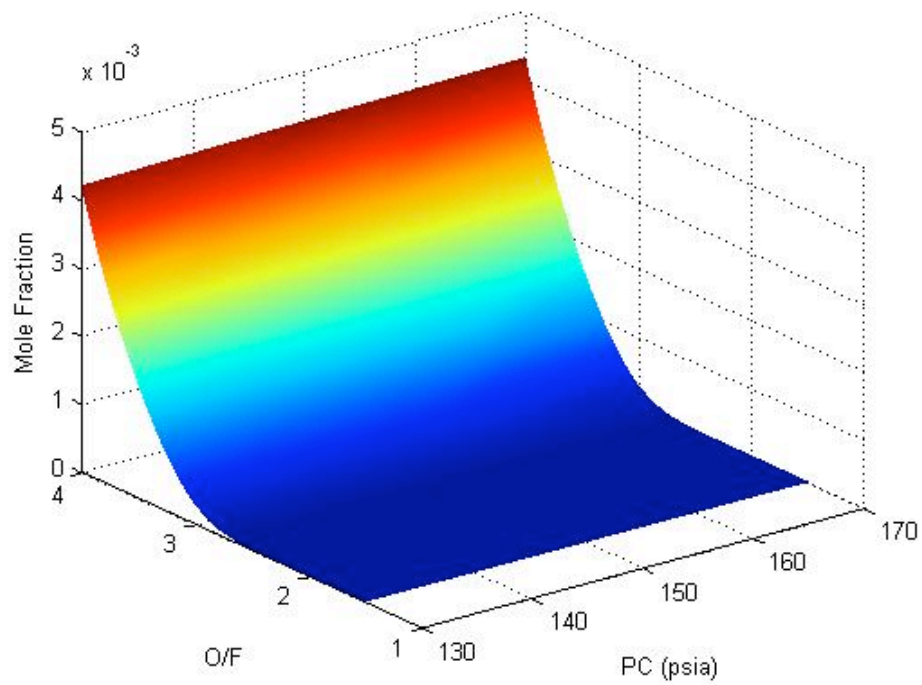


FIGURE 12. NO MOLE FRACTION AS A FUNCTION OF O/F RATIO AND CHAMBER PRESSURE

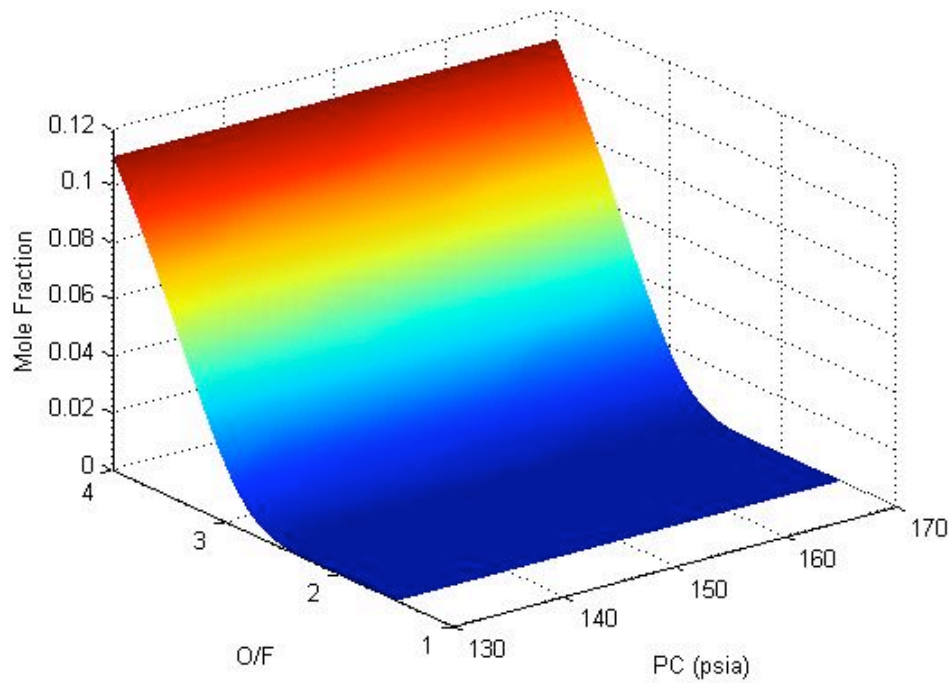


FIGURE 13. OH MOLE FRACTION AS A FUNCTION OF O/F RATIO AND CHAMBER PRESSURE

As the O/F ratio increases, the plume temperature, Fig. 14, increases. The presence of the OH band is attributed to the recombination of OH and H to H_2O .¹⁵ As the temperature of the plume rises, there is more thermal energy available to the kinetic chemistry of the conversion processes. The temperature output from the simulation results are taken from the chamber temperature values. These values are used because the stagnation temperature of the plume (mach diamond region) should equal the chamber temperature.

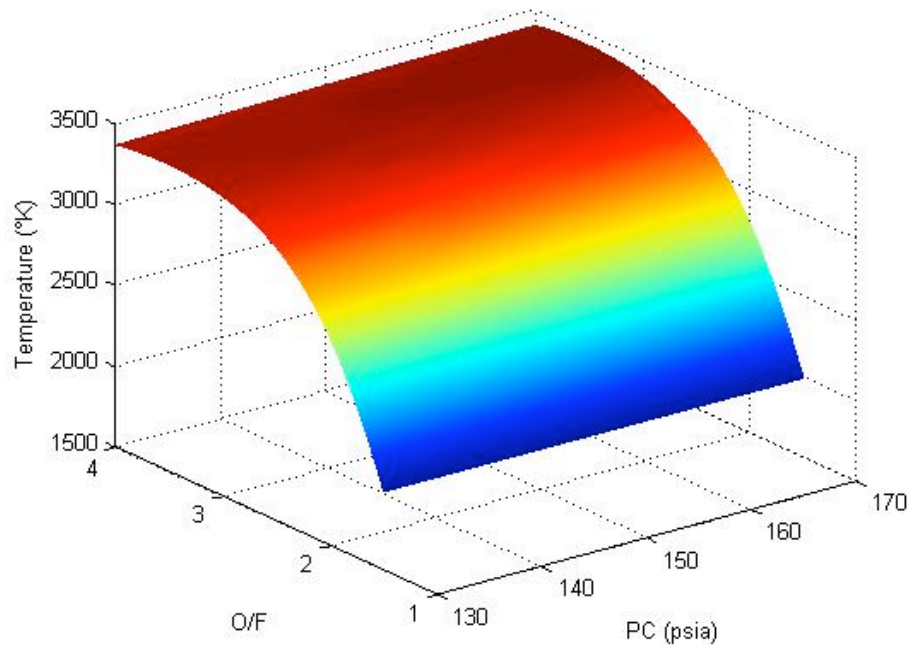


FIGURE 14. CHAMBER TEMPERATURE (°K) AS A FUNCTION OF O/F RATIO AND CHAMBER PRESSURE

The specific impulse (I_{sp}) of a propulsion system is the impulse (change in momentum) per unit of propellant. It is used as a measure of the efficiency of the propulsion system. In practice, the specific impulses of real engines vary somewhat with both altitude and thrust; nevertheless, I_{sp} is a useful value to compare engines; much like "miles per gallon" is used for cars.

Depending on whether the amount of propellant is expressed in mass or by weight (conventionally sea level weight on the Earth) the dimensions of specific impulse is either that of impulse per unit mass, or time, respectively, differing by a factor of g , the gravitational acceleration at the surface of the Earth.

Specific impulse is the change in momentum per unit mass for rocket fuels, or rather how much more push accumulates as you use that fuel. The speed of a rocket depends on thrust (which is roughly the amount of propellant that is thrown out of the back of the rocket and the speed at which that propellant is thrown out) compared to the rocket's weight.

The faster the speed at which propellant is thrown out the back of the rocket, the faster the rocket can travel or the more cargo it can carry. The specific impulse of a rocket propellant is a rough measure of how fast the propellant is ejected out of the back of the rocket. A rocket with a high specific impulse doesn't need as much fuel as a rocket with low specific impulse. The higher the specific impulse, the more push you get for the fuel that rushes out. Or, put another way, specific impulse determines how much fuel you have to use to get a good-sized push.

The mixture ratio generating the highest Isp for a given propellant combination is not necessarily the stoichiometric mixture ratio. Often, the highest Isp is generated under fuel rich conditions, which typically result in some unburned hydrogen in the exhaust. Even then, not all real-world engines are run at the optimum mixture ratio. A non-optimum ratio may be chosen to lower the chamber temperature to aid cooling of the combustion chamber and throat, or to minimize the use of bulky propellants such as liquid hydrogen. The calculated Isp of the thruster is shown in Fig. 15.

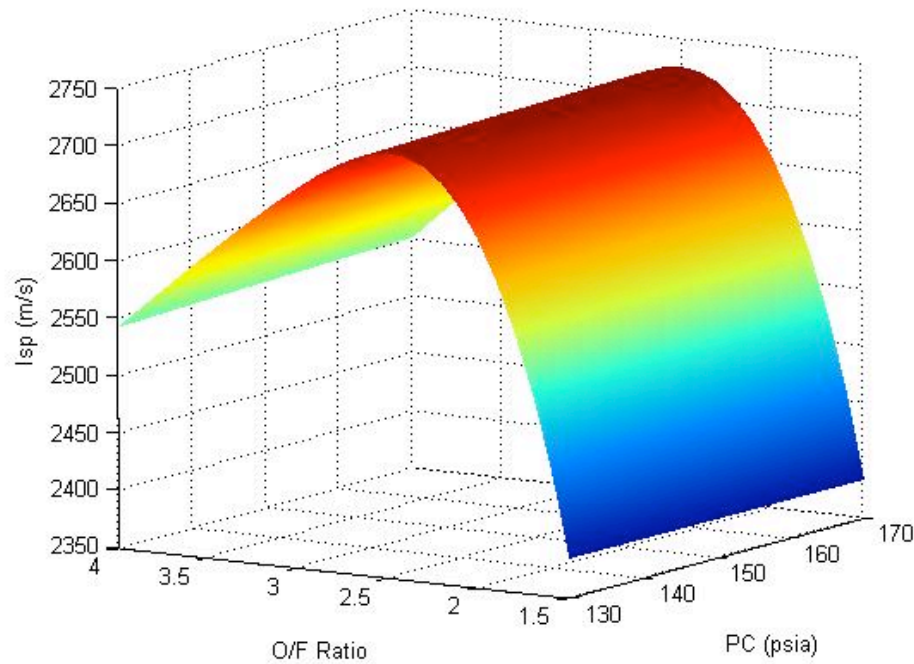


FIGURE 15. VARIATION IN SPECIFIC IMPULSE WITH CHANGE IN O/F RATIO AND CHAMBER PRESSURE

CFD Analysis

The output of the CEA code for engine operating parameters, 150 psia chamber pressure and an O/F of 1.8, was used as the initial values for the CRUNCH CFD code. The modeling process begins with the creation of a computational grid for the model. Taking in to account the axisymmetric geometry of the methane thruster, the plume was assumed to be axisymmetrical about the centerline of the engine. Using the Gridgen software program by Pointwise, Inc, a two-dimensional axisymmetric grid was generated. In order to help understand how the grid should be structured and to optimize the positioning of the mesh points at the computational boundaries, visible plume data was reviewed to judge the approximate plume structure, Fig. 16.¹⁷ It was estimated that the spreading rate

of the visible plume was at a half-angle of 5 to 6 degrees. To reduce the impact of the free-stream boundary condition on the predicted plume formation, the free-stream boundary was defined to have a parallel slope to match the estimated spreading rate of the plume, Fig.16 in blue. The boundary condition, in green in Fig. 16, imposed in the CFD code at the exit of the domain was an extrapolated boundary condition. The NASA CEA code computed the fixed-flux inlet conditions at the MTTP nozzle for use as the initializing parameters for the CRUNCH CFD code. The initial parameters chosen were the mixture oxidizer-to-fuel ratio and the stagnation chamber pressure. The final structured grid contained approximately 67,000 grid points.

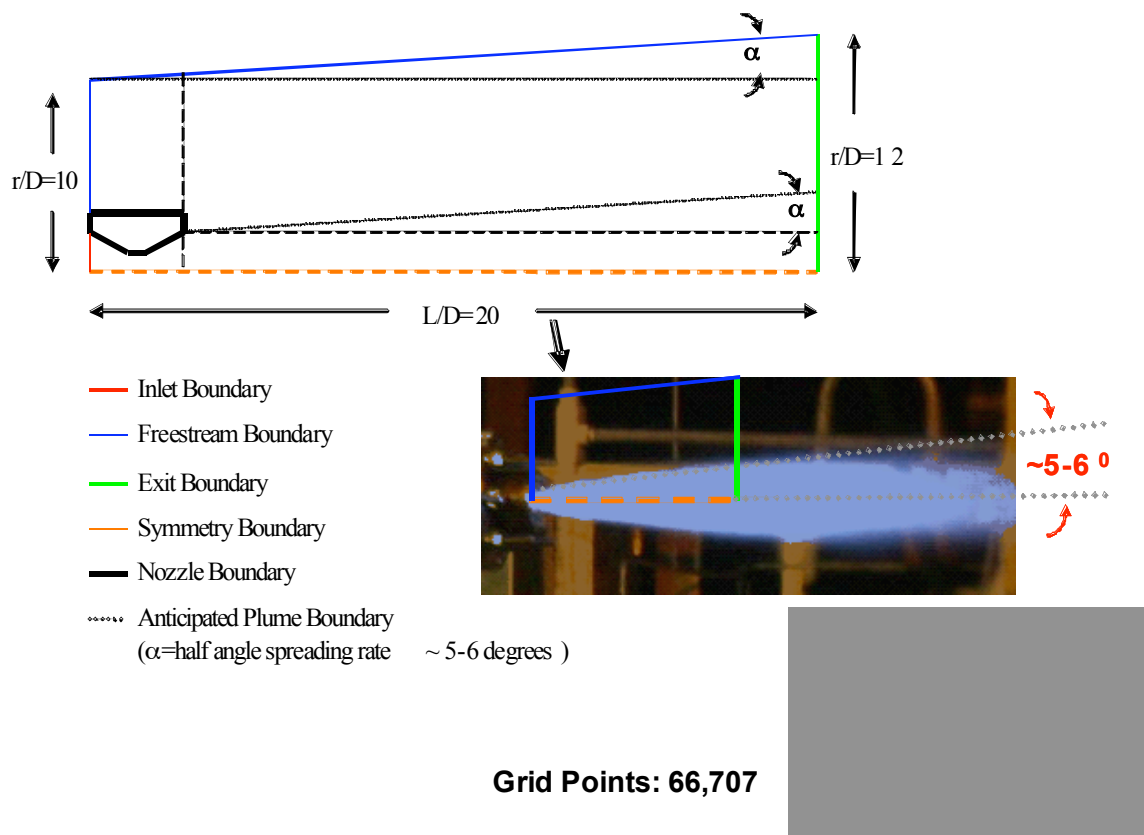


FIGURE 16. PLUME GEOMETRY FOR CFD GRID GENERATION.¹⁷

After the grid was completed, the PreCRUNCH program was run on the grid to decompose the grid for the number of processors specified in the input file. The model was run on the SSC Computational Cluster on 16 processors. After the model converges, that is, the plume has stabilized (meaning no movement in the position of the mach diamonds or in the plume turbulence) and there are no mass flow-rate errors (mass is conserved), the CRUNCH model results are run through the PostCRUNCH application. PostCRUNCH reassembles the domains and outputs a single result file in Tecplot format. Using Tecplot, the fluid properties of interest along the different Lines-Of-Sight (LOS) are extracted. These properties include: temperature, pressure, x-velocity, y-velocity, z-velocity, density, etc. Figure 17 shows the results of the CFD simulation for temperature. The black line imposed on the image is the LOS along which the fluid properties were extracted. Figure 18 illustrates a representative set of curves for the species CO and the temperature of the plume along the angled LOS. Figure 19 shows the plume temperature profile under the same conditions, with the imposed LOS perpendicular (\perp) to the centerline of the plume. Figure 20 is an example of the set of curves for the species CO and the temperature of the plume along the \perp LOS.

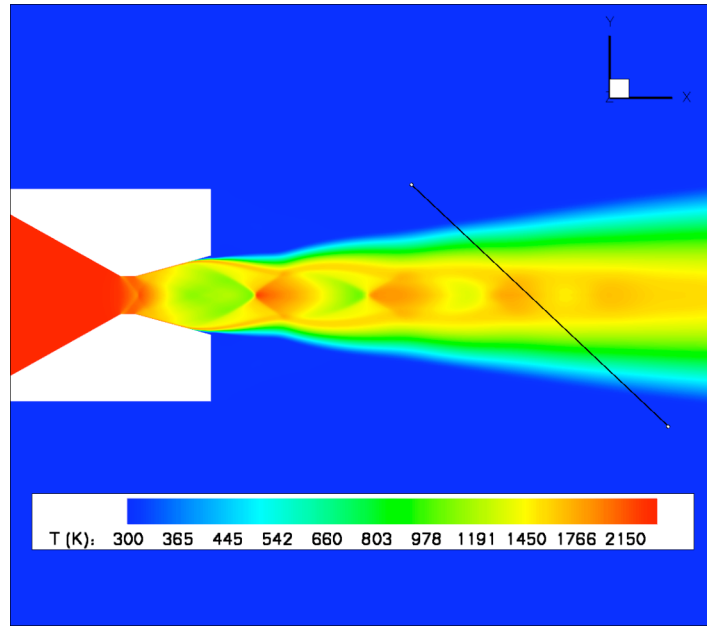


FIGURE 17. MTTP CFD TEMPERATURE PROFILE FOR O/F OF 1.8 AND PC OF 150 PSIA.

BLACK LINE INDICATES THE LOS USED TO EXTRACT SPECIES CONCENTRATIONS.¹⁷

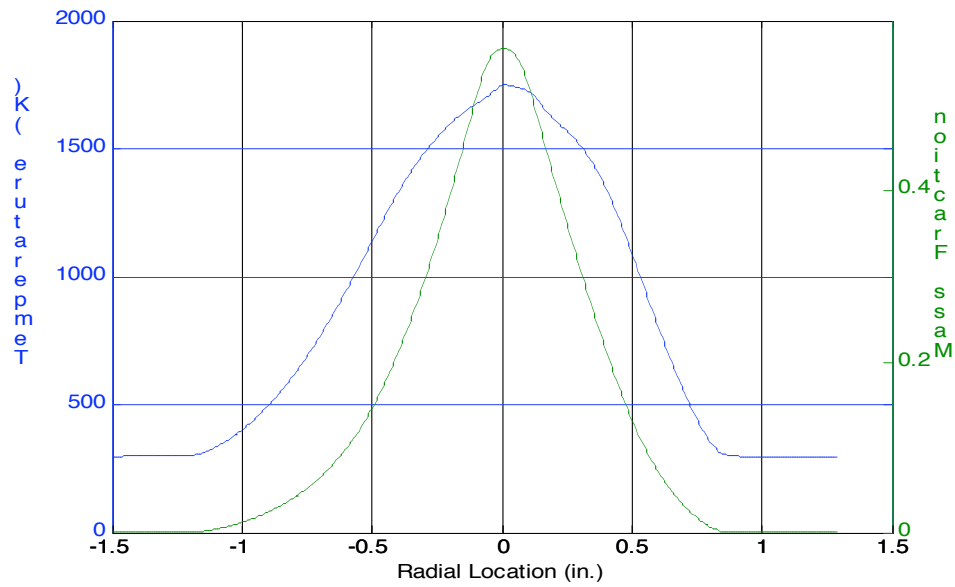


FIGURE 18. EXTRACTED DATA SHOWING PLUME CO MASS FRACTION CONCENTRATION

AND PLUME TEMPERATURE ALONG THE ANGLED LOS.¹⁷

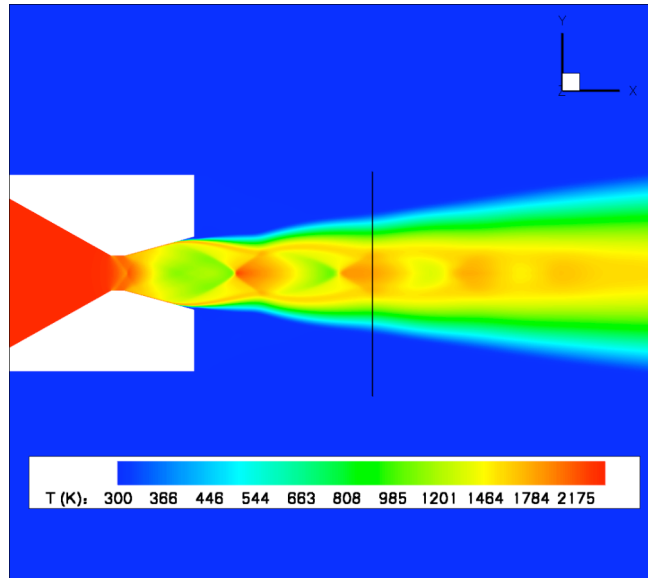


FIGURE 19. MTTP CFD TEMPERATURE PROFILE FOR O/F OF 1.8 AND PC OF 150 PSIA.

BLACK LINE INDICATES THE LOS USED TO EXTRACT SPECIES CONCENTRATIONS¹⁷

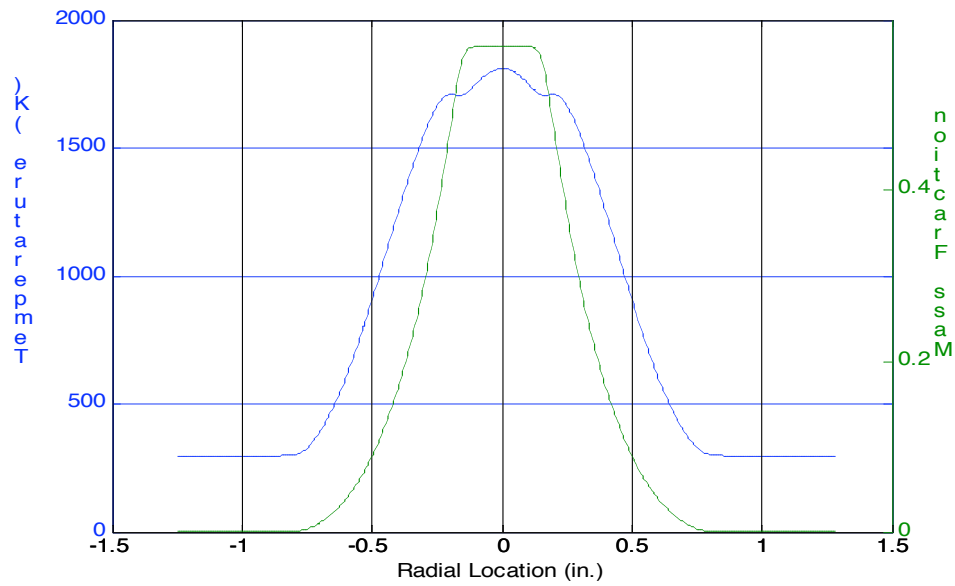


FIGURE 20. EXTRACTED DATA SHOWING PLUME CO MASS FRACTION CONCENTRATION

AND PLUME TEMPERATURE ALONG THE PERPENDICULAR LOS.¹⁷

The results of the computational analysis were used to facilitate the setup of the experimental optical system. The alignment of the spectral systems' collection optics was initially determined by the location of the mach diamond structures in the CFD analysis. This gave confidence that the optics were aligned to a relatively hot part of the plume which was conducive for the plume diagnostics test.

Experimental Results

Hot fire testing of the Methane Thruster Testbed Project (MTTP) test article started in March 2006. The first few series of tests were designed for establishing the proper operating parameters to ensure stable, repeatable operation from test to test. Variations in chamber pressure and oxidizer-to-fuel (O/F) ratios were investigated to determine the optimum engine performance parameters to provide high quality spectroscopic data. Engine run duration was incremented slowly over a series of tests to ensure that adequate test duration could be achieved for later introduction of dopants consisting of metallic species.³ It is planned for the dopants to be introduced into the engine combustion chamber, thereby seeding the exhaust plume for validation of a spectral simulation code being developed at SSC. The test numbering system used during the program will be used throughout this discussion.

The specific tests reviewed are representative of the results obtained during the whole test program. Toward the end of the test program, the LOS and FOV of the spectral systems were modified between test series to investigate the effect this modification would have

on the spectral signal collected. The data reviewed relating to the effects of variations in engine operating parameters was all acquired with the collection optics oriented in the same configuration, in a co-linear style (see Fig. 24).

The MTTP engine's parameters, i.e. chamber pressure, propellant flowrates, and O/F ratio, were adjusted so that test duration of sufficient duration was attained to allow engine combustion to reach steady-state operation, (see Appendix C). During testing of the thruster, the O/F ratios were varied from 1.75 to 4.0 to determine the optimum setting to maximize the plume signature for radicals and intermediate combustion products. Plume spectral data acquired during engine operation at the higher O/F ratios show marked decrease in emissions from the radicals under investigation. Figure 20 shows representative spectra, acquired with the Spec10 system, illustrating the effect of different O/F ratios, under constant chamber pressure, on the plume spectral signature. It was determined that the engine should be operated in a fuel-rich condition, i.e. lower O/F, to enhance the intermediate and transient products. Consequently, the thruster was operated in a fuel-rich condition with O/F's ranging from 1.6 and 2.2. This range of ratios provided the desired conditions for results shown here. It is also safer to operate in fuel-rich environment compared to oxidizer-rich environment. GOX and CH₄ propellant mass flowrates for the tests under discussion are shown in Appendix B. In order to compare each band system's strength from test to test, the area under the curves of the molecular radicals' band systems were integrated. These are shown in Table 1.

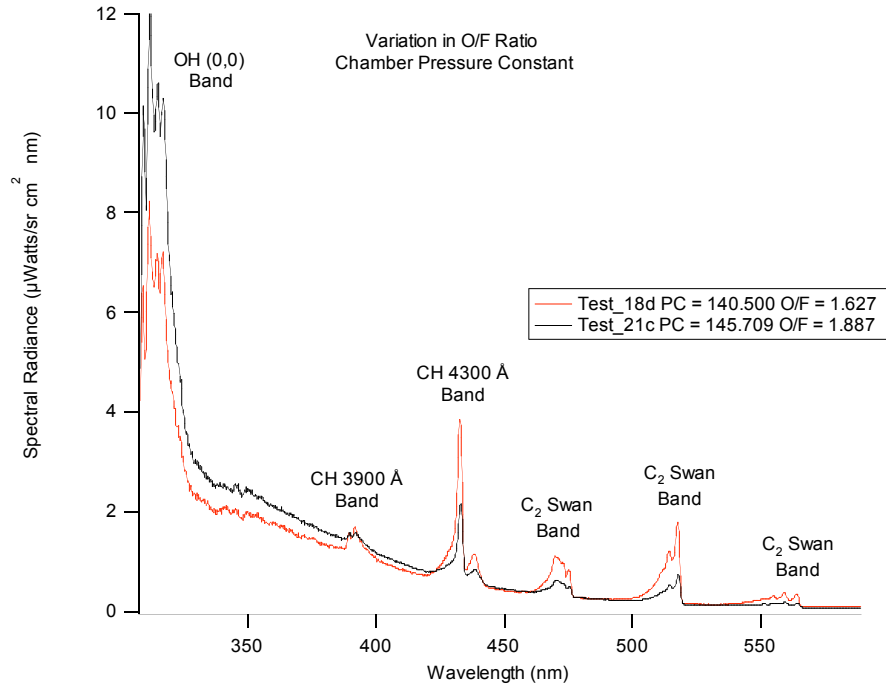


FIGURE 21. SPECTRA VARIATION WITH CHANGE IN O/F RATIO, CONSTANT CHAMBER PRESSURE

As a change in O/F usually resulted in a change in chamber pressure, there were no tests with exactly the same chamber pressure, yet different O/F ratios. The two tests (18D, 21C) chosen to illustrate the effect of changing O/F with constant chamber pressure had a very minor difference of less than 5 percent in chamber pressures. Although the difference in O/F was only 0.26, the increase had a noticeable effect on the monitored spectrum, Fig. 21. The area under the curve covering the spectral range of the individual band systems was integrated to determine the strength of the individual band systems, which will allow valid comparisons between tests. Table 1 shows comparisons of the individual bands systems. Test18D shows a higher spectral output across the band, when compared to Test 21C, except for the Hydroxyl (OH) band. The higher O/F of Test 21C produced a higher chamber temperature that accounts for the increased OH intensity, as

OH is highly temperature dependant. While the area of the OH band was over 106% higher during Test 21C than Test 18D, the intensity of the CH3900 Å band was ~47% higher during the test with the lower O/F, Test 18D. The CH4300 Å band showed a 56% reduction when the O/F was increased, and the C₂ Swan bands all showed ;lower band strengths of over 61% from Test 18D to Test 21C. The higher spectral band strengths of the carbon-based radicals can be attributed to the higher percentage of these transient species, despite the fact that band intensities of transient species also increase due to temperature.

Table 1. Molecular Band System Strength Comparison.

Test No.	Band System	Band System Beginning Wavelength	Band System Ending Wavelength	Band System Strength ($\mu\text{W}/\text{sr}\cdot\text{cm}^2$)	Percent Difference
18D 21C	OH	308.4	338.01	32.1522 66.3954	-106.50
18D 21C	CH 3900	388.86	397.1	1.63503 0.870671	46.75
18D 21C	CH 4300	420.91	443.81	13.6213 5.99013	56.02
18D 21C	C2 Swan	461.21	477.52	5.94896 2.31718	61.05
18D 21C	C2 Swan	497.34	520.65	9.94899 3.59857	63.83
18D 21C	C2 Swan	542.23	566.85	2.87399 0.960367	66.58

For the tests where the O/F ratio was kept constant and the chamber pressure was varied, Tests 20B and 20D were chosen, Fig 22. The band system strength comparison is shown in Table 2. While there was again a 2% change in chamber pressure, the change in O/F ratio was only 0.2%, compared with a change of over 14% for the previous data set. While the higher pressure of Test 20D produced more intensity in the OH radical band system (18.16% increase), the trend reversed itself as you go up the wavelength range. The intensity of the CH and C₂ bands systems was higher by up to 11% during Test 20B, which had a lower chamber pressure. The intensity profiles of the spectra were essentially the same, except for the OH radical. The higher OH is a function of the slightly higher temperature in the chamber.

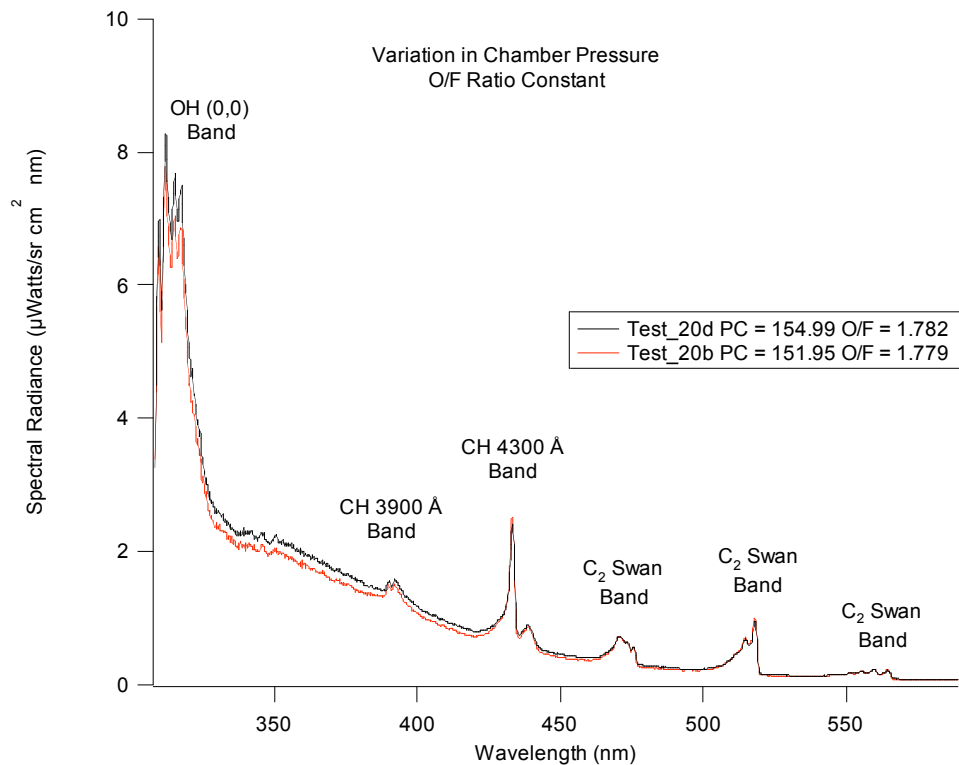


FIGURE 22. SPECTRA VARIATION WITH CHANGE IN CHAMBER PRESSURE, CONSTANT O/F RATIO

Table 2. Molecular Band System Strength Comparison

Test No.	Band System	Band System Beginning Wavelength	Band System Ending Wavelength	Band System Strength ($\mu\text{W}/\text{sr}\cdot\text{cm}^2$)	Percent Difference
20D 20B	OH	308.4	338.01	50.8144 41.5858	18.16
20D 20B	CH 3900	388.86	397.1	0.853179 0.820289	3.85
20D 20B	CH 4300	420.91	443.81	7.06136 7.85577	-11.25
20D 20B	C2 Swan	461.21	477.52	2.93037 3.15395	-7.63
20D 20B	C2 Swan	497.34	520.65	4.85324 5.19212	-6.98
20D 20B	C2 Swan	542.23	566.85	1.35228 1.50446	-11.25

The cumulative effect of increasing the O/F ratio and the chamber pressure can be seen in Fig. 23. Note that with an increase in O/F, the chamber pressure rises. This is due to the higher mass flow rates used to increase the O/F ratios. As the chamber pressure was raised, the stagnation temperature in the chamber increased. This was a direct result of the higher O/F, which implied more complete combustion was occurring. This had the effect of lowering the spectral band strength of all of the radicals under observation, except for the OH radical, which is strongly temperature dependant.

Variations in both engine parameters at the same time, different O/F and different chamber pressure), resulted in large changes from test to test in the spectral radiance of the band systems as shown in Fig 23. Tests 18D, 19F and 20E were chosen as representative of the ranges of engine parameters tested. Table 3 shows the comparison of the band systems' strength, along with the percent difference of band strength between the tests, with Test 18D as the baseline. The intensity of the OH band of Test 19F is significantly higher than that of the other tests, approximately 57% higher than Test 20E and 69% higher than Test 18D. The strong temperature dependence of the OH radical is the main variable that accounts for the relative strength of the OH band systems. Although the strength of the OH band is higher in the spectrum of Test 19F than either of the other tests, the spectral intensity of the other relevant band systems is lower. The band strength of the CH 3900 Å system is 20% smaller in Test 20E and 64% in Test 19F than the intensity of the band system in Test 18D. The strength of the CH 4300 Å band is significantly higher in Test 18D than in either of the other two tests, 45% lower in Test 20E and 61% lower in Test 19F. The band strengths of the three C₂ Swan band systems are similar, in that the intensity decreases as the O/F ratio increases, Table 3. The computational analysis with the CEA model shows in Figure 3, that as the O/F or chamber pressure was increased, the mole fraction of the C₂ increased after the O/F reached ~2.5. The analytical model assumes equilibrium conditions apply for the exhaust plume. This may account for the disparity between the analytical model and the spectral data.

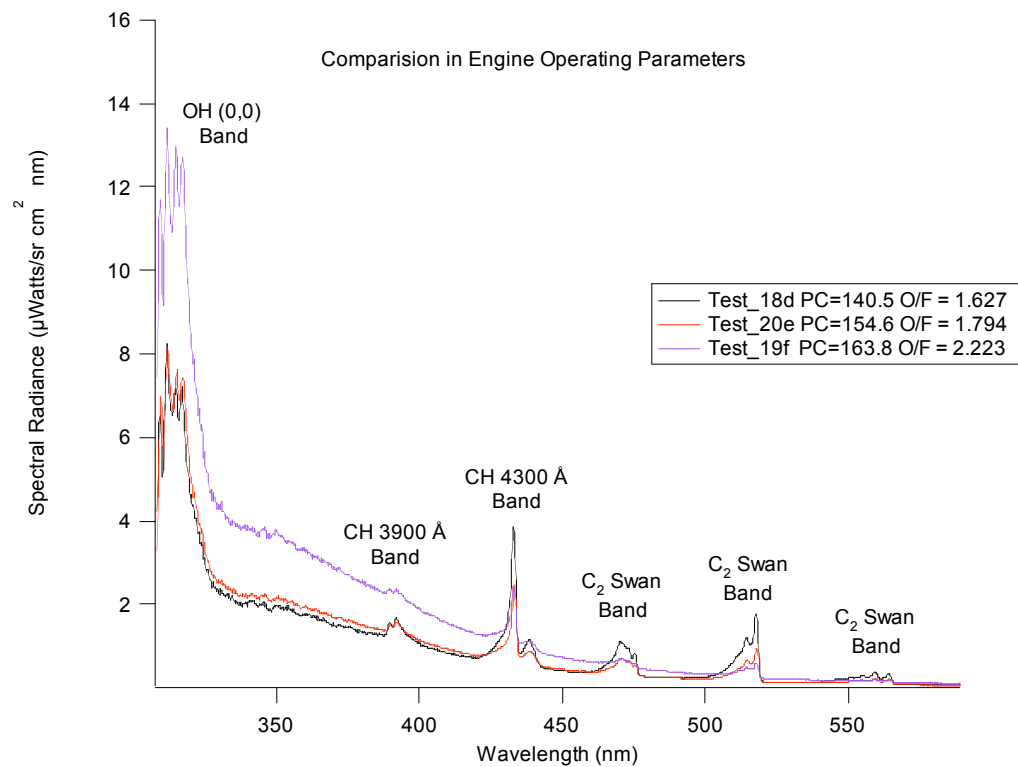


FIGURE 23. SPECTRA VARIATION WITH CHANGE IN ENGINE OPERATING PARAMETERS

Table 3.Molecular Band System Strength Comparison

Test No.	Band System	Band System Beginning Wavelength	Band System Ending Wavelength	Band System Strength ($\mu\text{W}/\text{sr}\cdot\text{cm}^2$)	Percent Difference
18D	OH	308.4	338.01	32.1522	
20E				50.6056	-57.39
19F				54.4309	-69.29
18D	CH 3900	388.86	397.1	1.07221	
20E				0.856703	20.10
19F				0.383727	64.21
18D	CH 4300	420.91	443.81	13.6213	
20E				7.47611	45.11
19F				5.26303	61.36
18D	C2 Swan	461.21	477.52	5.94896	
20E				2.90606	51.15
19F				1.3028	78.10
18D	C2 Swan	497.34	520.65	9.94899	
20E				4.87909	50.96
19F				2.12587	78.63
18D	C2 Swan	542.23	566.85	2.87399	
20E				1.40435	51.14
19F				0.552457	80.78

The optical system setup was modified during testing to determine the optimum configuration for the acquisition of quality plume data. During the first few series of tests, the collection optics for the spectral systems were configured in the same manner used in the collection of SSME data, namely, perpendicular to the plume centerline. The

collection optic is typically backlit with a Helium-Neon laser to aid in alignment and FOV focusing. The various optic locations are summarized in Table 4.

The collection optic was positioned approximately 155 in. from the exhaust plume centerline, perpendicular to the plume centerline, focused on the second Mach diamond 2.51 in. downstream of the nozzle exit plane. At these distances the collection system is focused to provide a 0.5 in. field of view (FOV). The collection optic was then moved to a location more co-linear with the plume, on top of the engine, aimed down through the plume in a semi coaxial manner, Fig.24 Several data series were acquired from this position, then the optic was moved to a position again perpendicular to the centerline, but at a much closer location, Fig.25.

Table 4. Collection Optic Alignment Orientation

Orientation to Plume	Test Number	X-Axial Distance@ centerline (in.)	Y-Axial Distance @ Centerline (in.)	Plume Pathlength (in.)
Perpendicular	12 D	155	2.51	2.47
Perpendicular	22 C	9.125	2.51	2.47
Co-Linear	21A	3.23 at 45°	3.84	4.4

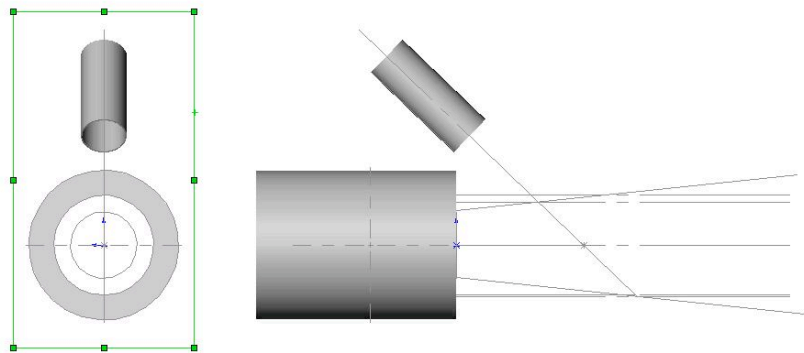


FIGURE 24. COLLECTION OPTIC CO-LINEAR CONFIGURATION FOR SPEC10 SYSTEM FOR TEST

SERIES 21

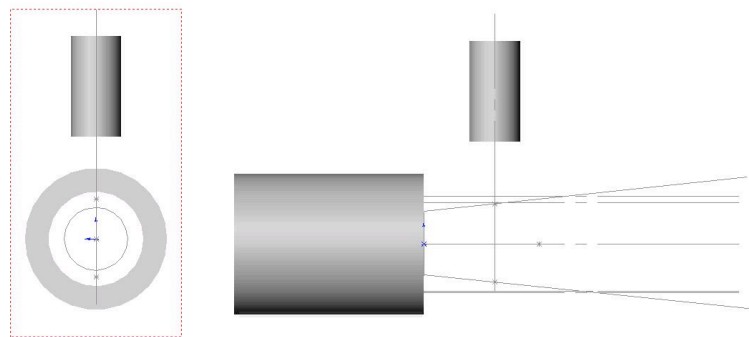


FIGURE 25. COLLECTION OPTIC PERPENDICULAR CONFIGURATION FOR SPEC10 SYSTEM FOR

TEST SERIES 22

Figure 26 shows the emission spectrum acquired during three representative tests with the Spec 10 spectrometer operating over a wavelength range of 300 to 580 nm. Characteristic

bands of emission observed for OH 3064 Å, CH 3900 Å, CH 4300 Å, and C₂ Swan are evident. The intensity of the spectra as a whole increased as the optic was moved closer, as would be expected. The increase in pathlength provided by angling the orientation of the optic also resulted in an increase in the spectral intensity of the molecular bands under study. The increase in the band strength attributed to the longer pathlength is no doubt due, in part, to the higher number of molecules available for emission, assuming a constant number density. Several other orientations were attempted, but the data was not usable. For example, the optic was positioned under the test article in a co-linear arrangement, but the spectral background of the clear sky was too intensive and saturated the detector. The angle of the co-linear alignment was increased for two tests, to investigate a longer pathlength. This produced spectra with no band systems visible. This is due to the LOS not passing through a mach diamond in the plume. The higher temperatures available in the Mach diamonds are essential to the production and detection of the transient radicals.

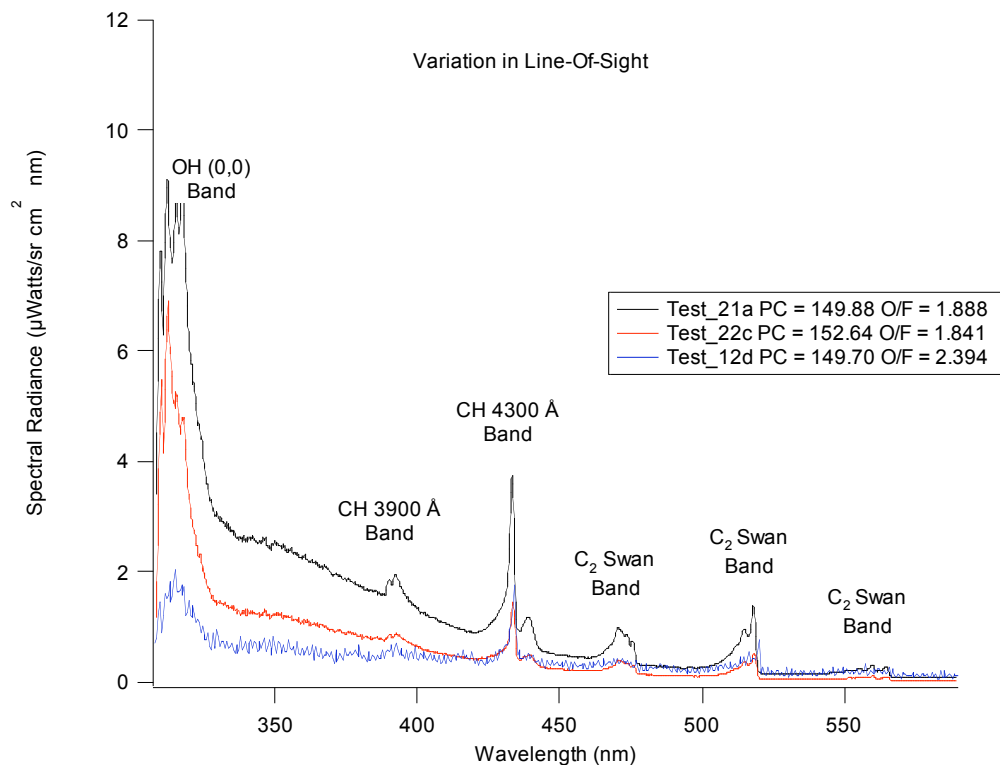


FIGURE 25. SPECTRA VARIATION WITH CHANGE IN LOS

The spectral band strength of the OH radical was 83% higher in Test 21A than that of Test 12D, Fig.23, and 19% higher than Test 22C, Table 4. The emission signature of CH 4300 Å band system is clearly visible in the spectrum from Test 21A, as is the relatively weak signatures of the CH 3900 Å band system. The signature for CH 4300 Å is noticeably reduced with the different optical alignment of Tests 22C and 12D and the weaker CH 3900 Å band system is almost undetectable from the noise in Test 12D. The percent difference for the spectral band strength shows that for the CH 3900 Å of Test 12D is actually higher than that of Test 22C. This could in part be due to a noisier signal from Test 12D, it might have skewed the integration slightly. The CH 4300 Å and the C₂ Swan band systems show percent differences in about the same range, CH 4300 Å about

64% lower and C₂ Swan about 64-74% lower. Again, the trend seems reversed for the highest wavelength C₂ Swan band, it shows less of a difference during Test 12D, compared to Test 21A, than that from Test 22C (Test 22C – 60%, Test 12D – 55%).

Table 5. Molecular Band System Strength Comparison

Test No.	Band System	Band System Beginning Wavelength	Band System Ending Wavelength	Band System Strength ($\mu\text{W}/\text{sr}\cdot\text{cm}^2$)	Percent Difference
21A	OH	308.4	338.01	64.738	
22C				52.2556	19.28
12D				10.3994	83.94
21A	CH 3900	388.86	397.1	1.79683	
22C				0.371869	79.30
12D				0.853556	52.50
21A	CH 4300	420.91	443.81	12.2629	
22C				4.33462	64.65
12D				4.41105	64.03
21A	C2 Swan	461.21	477.52	4.74616	
22C				1.69192	64.35
12D				1.32227	72.14
21A	C2 Swan	497.34	520.65	7.54786	
22C				2.84969	62.25
12D				1.91606	74.61
21A	C2 Swan	542.23	566.85	2.08379	
22C				0.822645	60.52
12D				0.929605	55.39

Chapter 5

CONCLUSIONS

The detection and identification of transient radicals produced during hotfire testing of a gaseous oxygen/gaseous methane fueled rocket engine through spectroscopic methods is easily possible with present day instrumentation. The ability to determine interference effects from C_2 , CH, CN, CO, and OH radicals experimentally ensures the application of Plume Diagnostics techniques to future hydrocarbon fueled rocket engine testing.

It is clear that interference from molecular bands in the spectral range of 300 to 850 nm will depend on several factors, such as O/F ratio, fuel composition, line-of-sight, and the spectral resolution, along with the engine power level. The O/F and LOS are the critical factors influencing the detection of the transient radicals. The more fuel-rich, lower O/F ratio, the more prominent the spectral characteristics of the radicals. The closer the collection optics is to the source, the higher the intensity of the detected spectra lines and the longer the optical path through the plume, the correspondingly higher the intensity of the band systems. The measurements undertaken during this work using the MTTP provides a better understanding of some of these effects. Future test series are planned to inject metallic dopants in the combustion chamber to determine interference effects from C_2 , CH, CN, CO and NO experimentally.

References

- ¹G. D. Tejjwani, F. E. Bircher, D. B. Van Dyke, G. P. McVay, C. D. Stewart, L. A. Langford, and C. C. Thurman, "Space Shuttle Main Engine Exhaust-Plume Spectroscopy", *Spectroscopy* 11(9), 31 (1996).
- ²G. D. Tejjwani, D. B. Van Dyke, F. E. Bircher, D. G. Gardner, and D. J. Chenevert, "Emission Spectra of Selected SSME Elements and Materials", NASA RP-1286, (1992).
- ³G. D. Tejjwani and C. C. Thurman, "Rocket Engine Plume Spectral Simulation and Quantitative Analysis", NASA Conference Publication 3282, Vol. I, Advanced Earth-to-Orbit Propulsion Technology, Huntsville, AL, May 17-19, 1994, pp. 200-214.
- ⁴F. E. Bircher, G. D. Tejjwani, E. L. Valenti, and C. C. Thurman, "Recent Results in the Development of the Engine Diagnostic Console", NASA Conference Publication 3282, Vol. I, Advanced Earth-to-Orbit Propulsion Technology, Huntsville, AL, May 17-19, 1994, pp. 190-199.
- ⁵G. D. Tejjwani, F. E. Bircher, D. B. Van Dyke, and C. C. Thurman, "Space Shuttle Main Engine Health Monitoring with Exhaust Plume Emission Spectroscopy", *Journal of Spacecraft and Rockets* 35, 387 (1998).
- ⁶G. P. McVay, F. E. Bircher, G. D. Tejjwani, and C. C. Thurman, "Development of an Atomic Absorption System for the Space Shuttle Main Engine", AIAA 97-2665, 33rd AIAA/ASME/SAE/ASEE Joint Propulsion Conference, Seattle, WA, July 6-9, 1997.
- ⁷G. D. Tejjwani, L. A. Langford, D. B. Van Dyke, G. P. McVay, and C. C. Thurman, "Rocket Engine Plume Diagnostics at Stennis Space Center", 27th JANNAF Exhaust Plume Technology Subcommittee Meeting, NASA Stennis Space Center, MS, May 5-9, 2003.
- ⁸G. D. Tejjwani, "Hydrocarbon-Fueled Rocket Engine Plume: Spectral Simulation, Phase I Report", Jacobs Sverdrup Technology, Inc, NASA Test Operations Group, Stennis Space Center, MS, December 30, 2005.
- ⁹G. D. Tejjwani, "Hydrocarbon-Fueled Rocket Engine Plume: Spectral Simulation, Phase II Report", Jacobs Sverdrup Technology, Inc., NASA Test Operations Group, Stennis Space Center, MS, to be published.
- ¹⁰F.S.Simmons, "Rocket Exhaust Plume Phenomenology," The Aerospace Press, El Segundo, CA. 2000
- ¹¹D. M. Cooper and R. W. Nicholls, "Measurements of the Electronic Transition Moments of C₂ Band System", *J. Quant. Spectrosc. Radiat. Transfer* 15, 139 (1975).
- ¹²R. Kepa, A. Para, M. Rytel, and M. Zachwieja, "New Spectroscopic Analysis of the B²Σ⁻ – X²Π Band System of the CH Molecule, *J. Mol. Spectrosc.* 178, 189 (1996).
- ¹³C. V. V. Prasad, and P. F. Bernath, "Fourier Transform Jet-Emission Spectroscopy of the Transition of CN", *J. Mol. Spectrosc.* 156, 327 (1992).
- ¹⁴G. D. Tejjwani, L. A. Langford, G. P. McVay, and W. W. St.Cyr "Hydrocarbon-Fueled Rocket Engine Plume Diagnostics: Analytical Development & Experimental Results", AIAA 2006-4407, 42nd AIAA/ASME/SAE/ASEE Joint Propulsion Conference & Exhibit, 9-12 July 2006, Sacramento, CA.
- ¹⁵G. H. Dieke and H. M. Crosswhite, "The Ultraviolet Bands of OH Fundamental Data", *J. Quant. Spectros. Radiant. Transfer* 2, 97 – 199 (1962)
- ¹⁶C. Th. J. Alkemade, R. Herrmann, "Fundamentals of Analytical Flame Spectroscopy", John Wiley & Sons, New York, 1979
- ¹⁷Dr. Daniel Allgood, , Jacobs Technology, Stennis Space Center, MS, Private Communication, October 2006
- ¹⁸Cavallo, P.A., and Grismer, M.J., "Further Extension And Validation Of A Parallel Unstructured Mesh Adaptation Package" Paper No. AIAA-2005-0924, 43rd Aerospace Sciences Meeting and Exhibit, Reno, NV, Jan. 10-13, 2005.

¹⁹Hosangadi, A., and Ahuja, V., “A New Unsteady Model for Dense, Cloud Cavitation in Cryogenic Fluids,” Paper No. AIAA-2005-5347, 17th Computational Fluids Dynamic Conference, Toronto, Ontario, CA, Jun. 6-9, 2005.

²⁰<http://www.craft-tech.com/html/crunch.html>

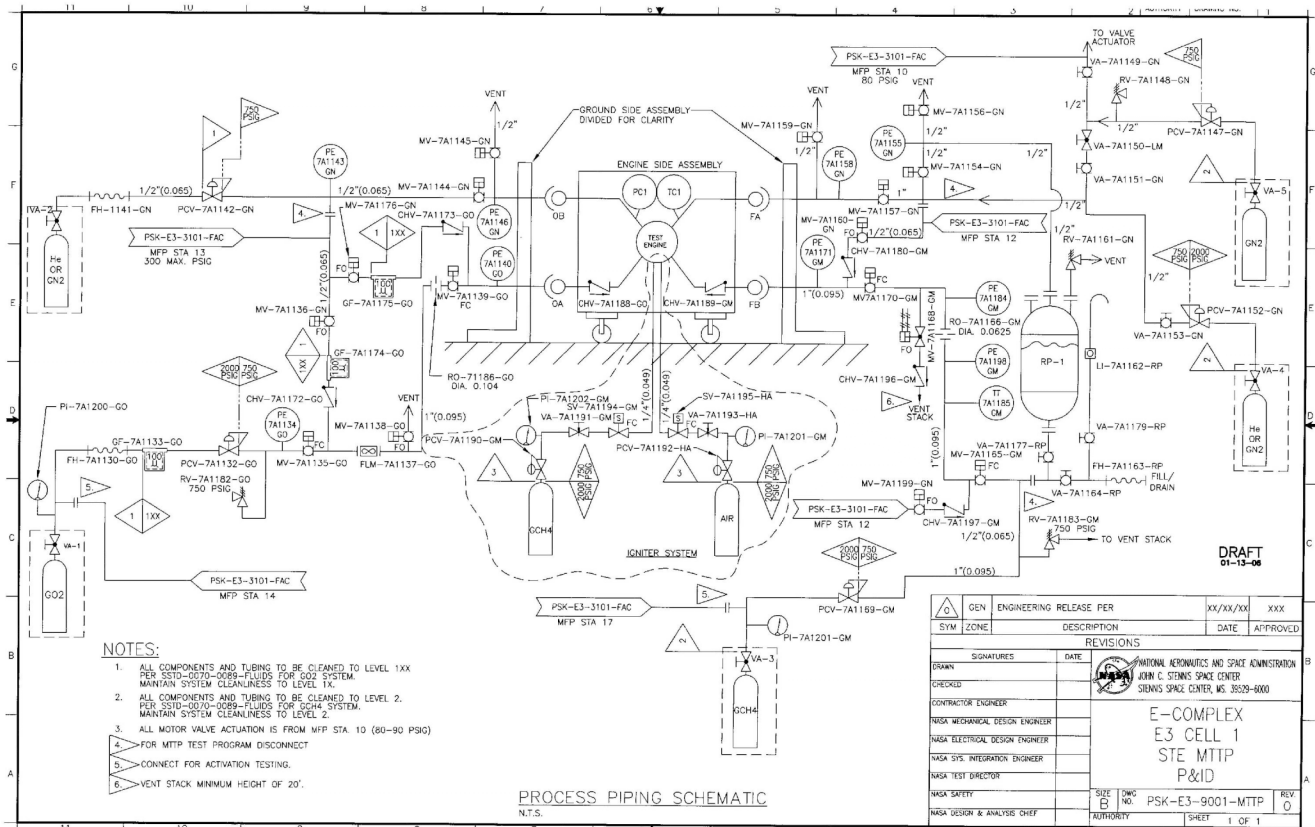
²¹S. Gordon and B.J. McBride, “Computer Program for Calculation of Complex Equilibrium Compositions and Applications. Part I Analysis”, NASA Reference Publication-1311, Part I, October 1994.

²²B.J. McBride and S. Gordon, “Computer Program for Calculation of Complex Equilibrium Compositions and Applications. Part II Users Manual and Program Description,” NASA Reference Publication-1311-P2, June 1996.

²³<http://www.grc.nasa.gov/WWW/CEAWeb>

²⁴A. H. Lefebvre, “Gas Turbine Combustion”, 2nd Edition, Taylor & Francis, Philadelphia, PA, 1999.

Appendix A – Methane Thruster Testbed P&ID



Appendix B - CEA O/F Input Files:

CEA Low O/F Input File

```
prob
ions
o/f=1.5,1.6,1.7,1.8,1.9,2.0,2.1,2.2,2.3,2.4,2.5,2.6,2.7,2.8,2.9,3.0
rocket fac ac/at=20.2 tcest,k=3800
p,psia=130,135,140,145,150,155,160,165,170
sup,ae/at=4.24
react
  oxid=O2 moles=100 t,k=298.15
  fuel=CH4 moles=100. t,k=298.15
  name=N2 moles=2
only
  C CH CH4 CN CO CO2 C2 C2H2 H H2 H2O N NCO NO N2 O OH C(gr) CO CO2 C2
  C2
  C2- CN CN- OH OH-
output
  trace=1E-30 siunits transport
end
```

CEA High O/F Input File:

```
prob
ions o/f=3.1,3.2,3.3,3.4,3.5,3.6,3.7,3.8,3.9,4.0
rocket fac ac/at=20.2 tcest,k=3800
p,psia=130,135,140,145,150,155,160,165,170
sup,ae/at=4.24
react
  oxid=O2 moles=100 t,k=298.15
  fuel=CH4 moles=100. t,k=298.15
  name=N2 moles=2
only
  C CH CH4 CN CO CO2 C2 C2H2 H H2 H2O N NCO NO N2 O OH C(gr) CO CO2 C2
  C2
  C2- CN CN- OH OH-
output
  trace=1E-30 siunits transport
end
```

Appendix C – Selected Engine Test Propellant Flowrates

Source	Parameter	Min	Max	Average
		lbs/s	lbs/s	lbs/s
0914-018A-6223-MTTP	GM_FLOW	0.050	0.052	0.051
0914-018A-6223-MTTP	GOX_FLOW	0.084	0.086	0.085
0914-018B-6223-MTTP	GM_FLOW	0.050	0.052	0.051
0914-018B-6223-MTTP	GOX_FLOW	0.083	0.086	0.084
0914-018c-6223-MTTP	GM_FLOW	0.050	0.051	0.051
0914-018c-6223-MTTP	GOX_FLOW	0.082	0.084	0.083
0914-018d-6223-MTTP	GM_FLOW	0.049	0.051	0.050
0914-018d-6223-MTTP	GOX_FLOW	0.081	0.084	0.082
0914-018e-6223-MTTP	GM_FLOW	0.049	0.050	0.049
0914-018e-6223-MTTP	GOX_FLOW	0.080	0.085	0.082
0914-019A-6230-MTTP	GM_FLOW	0.050	0.052	0.051
0914-019A-6230-MTTP	GOX_FLOW	0.088	0.091	0.089
0914-019B-6230-MTTP	GM_FLOW	0.050	0.051	0.051
0914-019B-6230-MTTP	GOX_FLOW	0.087	0.091	0.089
0914-019C-6230-MTTP	GM_FLOW	0.050	0.051	0.050
0914-019C-6230-MTTP	GOX_FLOW	0.088	0.090	0.089
0914-019d-6230-MTTP	GM_FLOW	0.049	0.050	0.050
0914-019d-6230-MTTP	GOX_FLOW	0.097	0.100	0.099
0914-019E-6230-MTTP	GM_FLOW	0.047	0.049	0.048
0914-019E-6230-MTTP	GOX_FLOW	0.096	0.099	0.097
0914-019F-6230-MTTP	GM_FLOW	0.042	0.046	0.044
0914-019F-6230-MTTP	GOX_FLOW	0.096	0.099	0.098
0914-020B-6255-MTTP	GM_FLOW	0.049	0.051	0.050
0914-020B-6255-MTTP	GOX_FLOW	0.088	0.090	0.089
0914-020C-6255-MTTP	GM_FLOW	0.050	0.051	0.050
0914-020C-6255-MTTP	GOX_FLOW	0.087	0.090	0.089
0914-020D-6255-MTTP	GM_FLOW	0.050	0.051	0.050
0914-020D-6255-MTTP	GOX_FLOW	0.089	0.092	0.091
0914-020E-6255-MTTP	GM_FLOW	0.049	0.050	0.050
0914-020E-6255-MTTP	GOX_FLOW	0.089	0.091	0.090
0914-021A-6262-MTTP	GM_FLOW	0.047	0.048	0.047
0914-021A-6262-MTTP	GOX_FLOW	0.088	0.090	0.089
0914-021B-6262-MTTP	GM_FLOW	0.047	0.048	0.047
0914-021B-6262-MTTP	GOX_FLOW	0.088	0.090	0.089
0914-021C-6262-MTTP	GM_FLOW	0.046	0.047	0.046
0914-021C-6262-MTTP	GOX_FLOW	0.086	0.088	0.087
0914-022A-6271-MTTP	GM_FLOW	0.049	0.050	0.049

0914-022A-6271-MTTP	GOX_FLOW	0.086	0.089	0.087
0914-022B-6271-MTTP	GM_FLOW	0.048	0.050	0.049
0914-022B-6271-MTTP	GOX_FLOW	0.090	0.092	0.091
0914-022C-6271-MTTP	GM_FLOW	0.048	0.049	0.049
0914-022C-6271-MTTP	GOX_FLOW	0.089	0.091	0.089
0914-022D-6271-MTTP	GM_FLOW	0.047	0.048	0.048
0914-022D-6271-MTTP	GOX_FLOW	0.086	0.089	0.087

Appendix D – CEA Output Results

Chamber Temperature as a function of O/F ratio and Chamber Pressure

T, K	130	135	140	145	150	155	160	165	170
1.5	1975.24	1975.28	1975.32	1975.35	1975.38	1975.41	1975.44	1975.47	1975.5
1.6	2167	2167.12	2167.23	2167.33	2167.44	2167.53	2167.62	2167.71	2167.8
1.7	2344.25	2344.54	2344.81	2345.07	2345.32	2345.55	2345.78	2346	2346.2
1.8	2505.14	2505.71	2506.26	2506.77	2507.26	2507.73	2508.18	2508.61	2509.02
1.9	2648.5	2649.45	2650.36	2651.22	2652.05	2652.84	2653.6	2654.33	2655.03
2.0	2774.22	2775.62	2776.96	2778.24	2779.47	2780.64	2781.77	2782.86	2783.9
2.1	2883.13	2885.02	2886.82	2888.55	2890.21	2891.8	2893.33	2894.8	2896.22
2.2	2976.61	2978.98	2981.24	2983.42	2985.51	2987.52	2989.46	2991.32	2993.13
2.3	3056.21	3059.03	3061.75	3064.35	3066.86	3069.27	3071.6	3073.84	3076.01
2.4	3123.5	3126.75	3129.87	3132.88	3135.77	3138.55	3141.24	3143.84	3146.36
2.5	3179.99	3183.62	3187.11	3190.47	3193.71	3196.84	3199.86	3202.78	3205.61
2.6	3227.06	3231.03	3234.85	3238.53	3242.07	3245.5	3248.81	3252.02	3255.13
2.7	3265.96	3270.23	3274.33	3278.28	3282.1	3285.79	3289.36	3292.81	3296.16
2.8	3297.81	3302.32	3306.67	3310.86	3314.91	3318.82	3322.61	3326.28	3329.84
2.9	3323.55	3328.27	3332.83	3337.22	3341.47	3345.57	3349.55	3353.4	3357.14
3.0	3344	3348.9	3353.63	3358.19	3362.6	3366.86	3371	3375	3378.89
3.1	3359.84	3364.89	3369.76	3374.46	3379	3383.4	3387.66	3391.79	3395.8
3.2	3371.64	3376.8	3381.78	3386.59	3391.25	3395.75	3400.11	3404.34	3408.45
3.3	3379.84	3385.1	3390.17	3395.06	3399.8	3404.39	3408.83	3413.14	3417.33
3.4	3384.82	3390.14	3395.28	3400.24	3405.04	3409.69	3414.19	3418.56	3422.81
3.5	3386.85	3392.22	3397.41	3402.41	3407.26	3411.95	3416.5	3420.91	3425.19
3.6	3386.16	3391.56	3396.77	3401.8	3406.67	3411.38	3415.96	3420.39	3424.7
3.7	3382.88	3388.29	3393.5	3398.55	3403.42	3408.14	3412.72	3417.17	3421.48
3.8	3377.1	3382.5	3387.7	3392.73	3397.6	3402.31	3406.88	3411.32	3415.62
3.9	3368.83	3374.19	3379.37	3384.37	3389.21	3393.9	3398.44	3402.85	3407.13
4.0	3358.01	3363.32	3368.45	3373.4	3378.19	3382.83	3387.33	3391.7	3395.94

Specie Mole Fraction as a function of O/F Ratio at a Chamber Pressure of 130 psig

130.0	C	CH	CN	CO	CO2	C2	NO	OH
1.5	2.694-31	1.666-27	1.812-20	2.4942-1	8.0548-2	4.168-36	5.156-17	5.568-13
1.6	9.133-29	1.502-25	3.171-19	2.5299-1	7.8062-2	8.258-34	2.505-15	1.481-11
1.7	3.813-26	1.594-23	6.256-18	2.5633-1	7.4790-2	2.043-31	1.355-13	4.247-10
1.8	6.244-24	8.132-22	7.745-17	2.5836-1	7.2768-2	2.138-29	3.984-12	7.2246-9
1.9	4.632-22	2.230-20	6.442-16	2.5906-1	7.2064-2	1.071-27	7.069-11	7.9888-8
2.0	1.827-20	3.722-19	3.894-15	2.5854-1	7.2578-2	2.973-26	8.435-10	6.2972-7
2.1	4.315-19	4.149-18	1.814-14	2.5689-1	7.4222-2	5.089-25	7.3263-9	3.7847-6
2.2	6.646-18	3.300-17	6.796-14	2.5412-1	7.6960-2	5.809-24	4.9023-8	1.8199-5
2.3	7.080-17	1.959-16	2.106-13	2.5021-1	8.0806-2	4.659-23	2.6292-7	7.2395-5
2.4	5.411-16	8.915-16	5.492-13	2.4504-1	8.5820-2	2.710-22	1.1599-6	2.4348-4
2.5	3.029-15	3.158-15	1.216-12	2.3849-1	9.2079-2	1.162-21	4.2762-6	7.0164-4
2.6	1.259-14	8.787-15	2.300-12	2.3041-1	9.9643-2	3.710-21	1.3309-5	1.7474-3
2.7	3.933-14	1.938-14	3.731-12	2.2075-1	1.0849-1	8.903-21	3.5271-5	3.7899-3
2.8	9.434-14	3.442-14	5.245-12	2.0959-1	1.1851-1	1.638-20	8.0515-5	7.2328-3
2.9	1.789-13	5.044-14	6.485-12	1.9714-1	1.2944-1	2.377-20	1.6074-4	1.2314-2
3.0	2.775-13	6.269-14	7.176-12	1.8371-1	1.4099-1	2.814-20	2.8578-4	1.9010-2
3.1	3.645-13	6.797-14	7.235-12	1.6962-1	1.5288-1	2.812-20	4.6129-4	2.7066-2
3.2	4.177-13	6.587-14	6.747-12	1.5517-1	1.6487-1	2.439-20	6.8849-4	3.6104-2
3.3	4.277-13	5.810-14	5.888-12	1.4057-1	1.7677-1	1.878-20	9.6551-4	4.5739-2
3.4	3.981-13	4.726-14	4.845-12	1.2598-1	1.8847-1	1.300-20	1.2893-3	5.5638-2
3.5	3.405-13	3.568-14	3.773-12	1.1155-1	1.9986-1	8.148-21	1.6570-3	6.5544-2
3.6	2.688-13	2.504-14	2.779-12	9.7344-2	2.1089-1	4.620-21	2.0671-3	7.5272-2
3.7	1.957-13	1.628-14	1.928-12	8.3462-2	2.2148-1	2.351-21	2.5200-3	8.4688-2
3.8	1.304-13	9.702-15	1.248-12	6.9980-2	2.3157-1	1.056-21	3.0189-3	9.3699-2
3.9	7.840-14	5.205-15	7.424-13	5.6987-2	2.4105-1	4.062-22	3.5707-3	1.0223-1
4.0	4.133-14	2.436-15	3.951-13	4.4597-2	2.4980-1	1.277-22	4.1878-3	1.1022-1

Specie Mole Fraction as a function of O/F Ratio at a Chamber Pressure of 135 psig

135.0	C	CH	CN	CO	CO2	C2	NO	OH
1.5	2.895-31	1.796-27	1.915-20	2.4945-1	8.0466-2	4.628-36	5.302-17	5.683-13
1.6	9.189-29	1.538-25	3.241-19	2.5299-1	7.8055-2	8.624-34	2.468-15	1.458-11
1.7	3.810-26	1.623-23	6.373-18	2.5633-1	7.4792-2	2.121-31	1.329-13	4.166-10
1.8	6.231-24	8.273-22	7.885-17	2.5835-1	7.2773-2	2.216-29	3.905-12	7.0826-9
1.9	4.615-22	2.266-20	6.552-16	2.5905-1	7.2072-2	1.109-27	6.923-11	7.8259-8
2.0	1.817-20	3.776-19	3.957-15	2.5853-1	7.2589-2	3.070-26	8.252-10	6.1634-7
2.1	4.283-19	4.203-18	1.841-14	2.5687-1	7.4238-2	5.246-25	7.1589-9	3.7010-6
2.2	6.587-18	3.339-17	6.892-14	2.5410-1	7.6979-2	5.978-24	4.7859-8	1.7783-5
2.3	7.010-17	1.980-16	2.134-13	2.5019-1	8.0827-2	4.790-23	2.5655-7	7.0711-5
2.4	5.358-16	9.012-16	5.567-13	2.4503-1	8.5840-2	2.787-22	1.1319-6	2.3785-4
2.5	3.005-15	3.197-15	1.234-12	2.3848-1	9.2097-2	1.197-21	4.1773-6	6.8600-4
2.6	1.252-14	8.917-15	2.337-12	2.3042-1	9.9657-2	3.831-21	1.3026-5	1.7112-3
2.7	3.930-14	1.973-14	3.799-12	2.2078-1	1.0851-1	9.233-21	3.4614-5	3.7198-3
2.8	9.475-14	3.519-14	5.355-12	2.0962-1	1.1852-1	1.707-20	7.9262-5	7.1173-3
2.9	1.806-13	5.176-14	6.638-12	1.9718-1	1.2947-1	2.488-20	1.5875-4	1.2149-2
3.0	2.813-13	6.453-14	7.361-12	1.8374-1	1.4104-1	2.956-20	2.8309-4	1.8801-2
3.1	3.707-13	7.015-14	7.433-12	1.6964-1	1.5296-1	2.962-20	4.5816-4	2.6824-2
3.2	4.258-13	6.809-14	6.940-12	1.5516-1	1.6498-1	2.575-20	6.8533-4	3.5844-2
3.3	4.369-13	6.014-14	6.061-12	1.4054-1	1.7692-1	1.984-20	9.6287-4	4.5474-2
3.4	4.071-13	4.894-14	4.988-12	1.2593-1	1.8865-1	1.375-20	1.2877-3	5.5379-2
3.5	3.484-13	3.695-14	3.884-12	1.1146-1	2.0008-1	8.614-21	1.6571-3	6.5301-2
3.6	2.751-13	2.593-14	2.859-12	9.7227-2	2.1114-1	4.880-21	2.0694-3	7.5050-2
3.7	2.002-13	1.684-14	1.982-12	8.3317-2	2.2176-1	2.479-21	2.5250-3	8.4491-2
3.8	1.333-13	1.002-14	1.281-12	6.9811-2	2.3187-1	1.110-21	3.0272-3	9.3530-2
3.9	7.995-14	5.363-15	7.605-13	5.6797-2	2.4137-1	4.256-22	3.5830-3	1.0209-1
4.0	4.202-14	2.501-15	4.034-13	4.4391-2	2.5014-1	1.330-22	4.2048-3	1.1011-1

Specie Mole Fraction as a function of O/F Ratio at a Chamber Pressure of 140 psig

140.0	C	CH	CN	CO	CO2	C2	NO	OH
1.5	3.109-31	1.933-27	2.021-20	2.4948-1	8.0385-2	5.126-36	5.453-17	5.801-13
1.6	9.248-29	1.574-25	3.311-19	2.5300-1	7.8048-2	8.996-34	2.433-15	1.437-11
1.7	3.808-26	1.652-23	6.488-18	2.5633-1	7.4794-2	2.198-31	1.305-13	4.090-10
1.8	6.219-24	8.412-22	8.021-17	2.5835-1	7.2777-2	2.294-29	3.830-12	6.9484-9
1.9	4.600-22	2.301-20	6.661-16	2.5904-1	7.2080-2	1.146-27	6.785-11	7.6723-8
2.0	1.808-20	3.830-19	4.018-15	2.5852-1	7.2601-2	3.168-26	8.079-10	6.0373-7
2.1	4.253-19	4.256-18	1.868-14	2.5686-1	7.4253-2	5.402-25	7.0016-9	3.6222-6
2.2	6.533-18	3.377-17	6.988-14	2.5409-1	7.6996-2	6.149-24	4.6777-8	1.7395-5
2.3	6.944-17	2.001-16	2.162-13	2.5017-1	8.0847-2	4.920-23	2.5056-7	6.9128-5
2.4	5.308-16	9.108-16	5.640-13	2.4501-1	8.5859-2	2.862-22	1.1056-6	2.3255-4
2.5	2.981-15	3.235-15	1.251-12	2.3848-1	9.2114-2	1.231-21	4.0840-6	6.7125-4
2.6	1.246-14	9.043-15	2.373-12	2.3043-1	9.9671-2	3.952-21	1.2758-5	1.6770-3
2.7	3.927-14	2.008-14	3.867-12	2.2080-1	1.0852-1	9.561-21	3.3989-5	3.6531-3
2.8	9.512-14	3.594-14	5.463-12	2.0966-1	1.1854-1	1.775-20	7.8065-5	7.0071-3
2.9	1.821-13	5.305-14	6.788-12	1.9721-1	1.2949-1	2.599-20	1.5683-4	1.1991-2
3.0	2.848-13	6.635-14	7.542-12	1.8377-1	1.4109-1	3.100-20	2.8048-4	1.8600-2
3.1	3.766-13	7.230-14	7.628-12	1.6966-1	1.5304-1	3.115-20	4.5511-4	2.6591-2
3.2	4.338-13	7.031-14	7.130-12	1.5516-1	1.6509-1	2.713-20	6.8225-4	3.5593-2
3.3	4.458-13	6.216-14	6.231-12	1.4051-1	1.7706-1	2.093-20	9.6027-4	4.5218-2
3.4	4.160-13	5.062-14	5.130-12	1.2587-1	1.8883-1	1.450-20	1.2862-3	5.5129-2
3.5	3.562-13	3.822-14	3.993-12	1.1137-1	2.0029-1	9.087-21	1.6571-3	6.5064-2
3.6	2.812-13	2.681-14	2.938-12	9.7113-2	2.1138-1	5.143-21	2.0715-3	7.4833-2
3.7	2.045-13	1.739-14	2.035-12	8.3177-2	2.2203-1	2.609-21	2.5298-3	8.4299-2
3.8	1.361-13	1.033-14	1.314-12	6.9646-2	2.3216-1	1.165-21	3.0352-3	9.3364-2
3.9	8.146-14	5.518-15	7.782-13	5.6613-2	2.4168-1	4.452-22	3.5948-3	1.0195-1
4.0	4.269-14	2.565-15	4.115-13	4.4192-2	2.5046-1	1.384-22	4.2212-3	1.1000-1

Specie Mole Fraction as a function of O/F Ratio at a Chamber Pressure of 145 psig

145.0	C	CH	CN	CO	CO2	C2	NO	OH
1.5	3.334-31	2.078-27	2.131-20	2.4951-1	8.0306-2	5.665-36	5.608-17	5.922-13
1.6	9.308-29	1.610-25	3.381-19	2.5300-1	7.8041-2	9.374-34	2.401-15	1.417-11
1.7	3.806-26	1.681-23	6.600-18	2.5632-1	7.4796-2	2.275-31	1.282-13	4.018-10
1.8	6.208-24	8.549-22	8.155-17	2.5834-1	7.2781-2	2.371-29	3.760-12	6.8215-9
1.9	4.585-22	2.336-20	6.767-16	2.5904-1	7.2087-2	1.183-27	6.654-11	7.5271-8
2.0	1.799-20	3.882-19	4.078-15	2.5851-1	7.2611-2	3.265-26	7.916-10	5.9183-7
2.1	4.225-19	4.308-18	1.894-14	2.5685-1	7.4267-2	5.557-25	6.8534-9	3.5479-6
2.2	6.480-18	3.414-17	7.080-14	2.5407-1	7.7014-2	6.315-24	4.5746-8	1.7026-5
2.3	6.881-17	2.021-16	2.190-13	2.5015-1	8.0866-2	5.048-23	2.4493-7	6.7636-5
2.4	5.261-16	9.201-16	5.712-13	2.4500-1	8.5878-2	2.937-22	1.0809-6	2.2755-4
2.5	2.959-15	3.271-15	1.268-12	2.3847-1	9.2130-2	1.265-21	3.9959-6	6.5731-4
2.6	1.240-14	9.166-15	2.408-12	2.3043-1	9.9684-2	4.071-21	1.2504-5	1.6445-3
2.7	3.924-14	2.041-14	3.932-12	2.2082-1	1.0853-1	9.888-21	3.3393-5	3.5897-3
2.8	9.547-14	3.667-14	5.569-12	2.0969-1	1.1855-1	1.844-20	7.6918-5	6.9018-3
2.9	1.836-13	5.432-14	6.935-12	1.9725-1	1.2952-1	2.710-20	1.5499-4	1.1840-2
3.0	2.883-13	6.814-14	7.721-12	1.8380-1	1.4114-1	3.244-20	2.7797-4	1.8406-2
3.1	3.824-13	7.443-14	7.821-12	1.6967-1	1.5311-1	3.269-20	4.5214-4	2.6366-2
3.2	4.416-13	7.250-14	7.319-12	1.5516-1	1.6520-1	2.852-20	6.7924-4	3.5350-2
3.3	4.546-13	6.418-14	6.400-12	1.4048-1	1.7720-1	2.203-20	9.5771-4	4.4969-2
3.4	4.246-13	5.229-14	5.270-12	1.2581-1	1.8900-1	1.527-20	1.2846-3	5.4886-2
3.5	3.638-13	3.948-14	4.102-12	1.1129-1	2.0050-1	9.567-21	1.6570-3	6.4835-2
3.6	2.873-13	2.768-14	3.017-12	9.7002-2	2.1162-1	5.411-21	2.0735-3	7.4622-2
3.7	2.088-13	1.795-14	2.087-12	8.3041-2	2.2229-1	2.740-21	2.5343-3	8.4111-2
3.8	1.388-13	1.065-14	1.346-12	6.9487-2	2.3245-1	1.221-21	3.0429-3	9.3203-2
3.9	8.294-14	5.672-15	7.956-13	5.6434-2	2.4199-1	4.648-22	3.6062-3	1.0182-1
4.0	4.334-14	2.627-15	4.195-13	4.3999-2	2.5077-1	1.437-22	4.2370-3	1.0989-1

Specie Mole Fraction as a function of O/F Ratio at a Chamber Pressure of 150 psig

150.0	C	CH	CN	CO	CO2	C2	NO	OH
1.5	3.57E-31	2.23E-27	2.24E-20	2.50E-01	8.02E-02	6.25E-36	5.77E-17	6.05E-13
1.6	9.37E-29	1.65E-25	3.45E-19	2.53E-01	7.80E-02	9.76E-34	2.37E-15	1.40E-11
1.7	3.80E-26	1.71E-23	6.71E-18	2.56E-01	7.48E-02	2.35E-31	1.26E-13	3.95E-10
1.8	6.20E-24	8.68E-22	8.29E-17	2.58E-01	7.28E-02	2.45E-29	3.69E-12	6.70E-09
1.9	4.57E-22	2.37E-20	6.87E-16	2.59E-01	7.21E-02	1.22E-27	6.53E-11	7.39E-08
2.0	1.79E-20	3.93E-19	4.14E-15	2.59E-01	7.26E-02	3.36E-26	7.76E-10	5.81E-07
2.1	4.20E-19	4.36E-18	1.92E-14	2.57E-01	7.43E-02	5.71E-25	6.71E-09	3.48E-06
2.2	6.43E-18	3.45E-17	7.17E-14	2.54E-01	7.70E-02	6.48E-24	4.48E-08	1.67E-05
2.3	6.82E-17	2.04E-16	2.22E-13	2.50E-01	8.09E-02	5.18E-23	2.40E-07	6.62E-05
2.4	5.22E-16	9.29E-16	5.78E-13	2.45E-01	8.59E-02	3.01E-22	1.06E-06	2.23E-04
2.5	2.94E-15	3.31E-15	1.28E-12	2.38E-01	9.21E-02	1.30E-21	3.91E-06	6.44E-04
2.6	1.23E-14	9.29E-15	2.44E-12	2.30E-01	9.97E-02	4.19E-21	1.23E-05	1.61E-03
2.7	3.92E-14	2.07E-14	4.00E-12	2.21E-01	1.09E-01	1.02E-20	3.28E-05	3.53E-03
2.8	9.58E-14	3.74E-14	5.67E-12	2.10E-01	1.19E-01	1.91E-20	7.58E-05	6.80E-03
2.9	1.85E-13	5.56E-14	7.08E-12	1.97E-01	1.30E-01	2.82E-20	1.53E-04	1.17E-02
3.0	2.92E-13	6.99E-14	7.90E-12	1.84E-01	1.41E-01	3.39E-20	2.76E-04	1.82E-02
3.1	3.88E-13	7.65E-14	8.01E-12	1.70E-01	1.53E-01	3.42E-20	4.49E-04	2.61E-02
3.2	4.49E-13	7.47E-14	7.51E-12	1.55E-01	1.65E-01	2.99E-20	6.76E-04	3.51E-02
3.3	4.63E-13	6.62E-14	6.57E-12	1.40E-01	1.77E-01	2.32E-20	9.55E-04	4.47E-02
3.4	4.33E-13	5.40E-14	5.41E-12	1.26E-01	1.89E-01	1.61E-20	1.28E-03	5.46E-02
3.5	3.71E-13	4.07E-14	4.21E-12	1.11E-01	2.01E-01	1.01E-20	1.66E-03	6.46E-02
3.6	2.93E-13	2.86E-14	3.10E-12	9.69E-02	2.12E-01	5.68E-21	2.08E-03	7.44E-02
3.7	2.13E-13	1.85E-14	2.14E-12	8.29E-02	2.23E-01	2.87E-21	2.54E-03	8.39E-02
3.8	1.41E-13	1.10E-14	1.38E-12	6.93E-02	2.33E-01	1.28E-21	3.05E-03	9.30E-02
3.9	8.44E-14	5.83E-15	8.13E-13	5.63E-02	2.42E-01	4.85E-22	3.62E-03	1.02E-01
4.0	4.40E-14	2.69E-15	4.27E-13	4.38E-02	2.51E-01	1.49E-22	4.25E-03	1.10E-01

Specie Mole Fraction as a function of O/F Ratio at a Chamber Pressure of 155 psig

155.0	C	CH	CN	CO	CO2	C2	NO	OH
1.5	3.822-31	2.390-27	2.360-20	2.4957-1	8.0151-2	6.874-36	5.929-17	6.171-13
1.6	9.437-29	1.682-25	3.519-19	2.5300-1	7.8026-2	1.015-33	2.343-15	1.381-11
1.7	3.802-26	1.737-23	6.821-18	2.5632-1	7.4799-2	2.430-31	1.239-13	3.884-10
1.8	6.187-24	8.815-22	8.417-17	2.5834-1	7.2789-2	2.526-29	3.629-12	6.5870-9
1.9	4.558-22	2.403-20	6.974-16	2.5902-1	7.2100-2	1.257-27	6.413-11	7.2591-8
2.0	1.782-20	3.984-19	4.196-15	2.5849-1	7.2631-2	3.458-26	7.615-10	5.6991-7
2.1	4.173-19	4.410-18	1.946-14	2.5682-1	7.4294-2	5.867-25	6.5812-9	3.4112-6
2.2	6.381-18	3.486-17	7.259-14	2.5404-1	7.7046-2	6.646-24	4.3856-8	1.6348-5
2.3	6.764-17	2.061-16	2.243-13	2.5012-1	8.0902-2	5.303-23	2.3459-7	6.4894-5
2.4	5.172-16	9.381-16	5.850-13	2.4497-1	8.5913-2	3.085-22	1.0353-6	2.1836-4
2.5	2.916-15	3.342-15	1.300-12	2.3846-1	9.2162-2	1.332-21	3.8335-6	6.3158-4
2.6	1.229-14	9.402-15	2.476-12	2.3044-1	9.9710-2	4.308-21	1.2034-5	1.5844-3
2.7	3.916-14	2.106-14	4.059-12	2.2085-1	1.0855-1	1.054-20	3.2283-5	3.4715-3
2.8	9.609-14	3.809-14	5.774-12	2.0974-1	1.1858-1	1.980-20	7.4763-5	6.7043-3
2.9	1.863-13	5.679-14	7.221-12	1.9731-1	1.2957-1	2.934-20	1.5150-4	1.1554-2
3.0	2.949-13	7.166-14	8.071-12	1.8386-1	1.4123-1	3.537-20	2.7318-4	1.8041-2
3.1	3.935-13	7.862-14	8.200-12	1.6970-1	1.5325-1	3.581-20	4.4645-4	2.5938-2
3.2	4.565-13	7.684-14	7.689-12	1.5515-1	1.6540-1	3.137-20	6.7340-4	3.4886-2
3.3	4.716-13	6.816-14	6.732-12	1.4042-1	1.7747-1	2.428-20	9.5268-4	4.4494-2
3.4	4.415-13	5.560-14	5.547-12	1.2571-1	1.8933-1	1.685-20	1.2814-3	5.4419-2
3.5	3.786-13	4.199-14	4.316-12	1.1113-1	2.0089-1	1.055-20	1.6567-3	6.4393-2
3.6	2.990-13	2.942-14	3.172-12	9.6790-2	2.1207-1	5.955-21	2.0770-3	7.4217-2
3.7	2.172-13	1.904-14	2.191-12	8.2780-2	2.2279-1	3.007-21	2.5428-3	8.3750-2
3.8	1.440-13	1.126-14	1.409-12	6.9183-2	2.3299-1	1.334-21	3.0573-3	9.2891-2
3.9	8.580-14	5.975-15	8.296-13	5.6093-2	2.4256-1	5.043-22	3.6277-3	1.0156-1
4.0	4.459-14	2.750-15	4.349-13	4.3631-2	2.5137-1	1.544-22	4.2672-3	1.0969-1

Specie Mole Fraction as a function of O/F Ratio at a Chamber Pressure of 160 psig

160.0	C	CH	CN	CO	CO2	C2	NO	OH
1.5	4.086-31	2.558-27	2.480-20	2.4959-1	8.0076-2	7.549-36	6.094-17	6.299-13
1.6	9.505-29	1.718-25	3.589-19	2.5300-1	7.8018-2	1.055-33	2.317-15	1.365-11
1.7	3.801-26	1.764-23	6.928-18	2.5632-1	7.4800-2	2.507-31	1.219-13	3.822-10
1.8	6.177-24	8.945-22	8.544-17	2.5833-1	7.2792-2	2.604-29	3.569-12	6.4783-9
1.9	4.545-22	2.436-20	7.075-16	2.5902-1	7.2106-2	1.294-27	6.302-11	7.1351-8
2.0	1.775-20	4.034-19	4.254-15	2.5848-1	7.2640-2	3.554-26	7.477-10	5.5978-7
2.1	4.148-19	4.459-18	1.971-14	2.5681-1	7.4306-2	6.021-25	6.4557-9	3.3481-6
2.2	6.334-18	3.521-17	7.346-14	2.5403-1	7.7061-2	6.811-24	4.2986-8	1.6035-5
2.3	6.710-17	2.080-16	2.269-13	2.5011-1	8.0918-2	5.430-23	2.2983-7	6.3630-5
2.4	5.130-16	9.468-16	5.918-13	2.4496-1	8.5930-2	3.158-22	1.0144-6	2.1411-4
2.5	2.896-15	3.376-15	1.316-12	2.3845-1	9.2177-2	1.365-21	3.7585-6	6.1968-4
2.6	1.223-14	9.516-15	2.509-12	2.3045-1	9.9722-2	4.424-21	1.1815-5	1.5564-3
2.7	3.911-14	2.137-14	4.121-12	2.2087-1	1.0857-1	1.086-20	3.1764-5	3.4163-3
2.8	9.636-14	3.877-14	5.874-12	2.0977-1	1.1860-1	2.048-20	7.3749-5	6.6116-3
2.9	1.876-13	5.799-14	7.361-12	1.9734-1	1.2960-1	3.046-20	1.4985-4	1.1419-2
3.0	2.980-13	7.339-14	8.243-12	1.8388-1	1.4127-1	3.684-20	2.7089-4	1.7867-2
3.1	3.988-13	8.069-14	8.385-12	1.6972-1	1.5332-1	3.740-20	4.4371-4	2.5735-2
3.2	4.637-13	7.899-14	7.871-12	1.5514-1	1.6549-1	3.281-20	6.7057-4	3.4665-2
3.3	4.798-13	7.014-14	6.896-12	1.4040-1	1.7759-1	2.542-20	9.5022-4	4.4266-2
3.4	4.497-13	5.724-14	5.683-12	1.2566-1	1.8949-1	1.765-20	1.2798-3	5.4196-2
3.5	3.859-13	4.324-14	4.422-12	1.1105-1	2.0107-1	1.105-20	1.6565-3	6.4181-2
3.6	3.048-13	3.028-14	3.248-12	9.6689-2	2.1228-1	6.233-21	2.0787-3	7.4022-2
3.7	2.213-13	1.958-14	2.242-12	8.2655-2	2.2303-1	3.143-21	2.5468-3	8.3576-2
3.8	1.466-13	1.157-14	1.440-12	6.9037-2	2.3325-1	1.391-21	3.0641-3	9.2740-2
3.9	8.718-14	6.124-15	8.462-13	5.5929-2	2.4284-1	5.241-22	3.6380-3	1.0144-1
4.0	4.519-14	2.809-15	4.423-13	4.3455-2	2.5166-1	1.596-22	4.2816-3	1.0959-1

Specie Mole Fraction as a function of O/F Ratio at a Chamber Pressure of 165 psig

165.0	C	CH	CN	CO	CO2	C2	NO	OH
1.5	4.363-31	2.734-27	2.603-20	2.4962-1	8.0002-2	8.274-36	6.263-17	6.429-13
1.6	9.575-29	1.755-25	3.658-19	2.5300-1	7.8010-2	1.095-33	2.293-15	1.349-11
1.7	3.800-26	1.791-23	7.035-18	2.5632-1	7.4802-2	2.584-31	1.200-13	3.763-10
1.8	6.168-24	9.072-22	8.670-17	2.5833-1	7.2796-2	2.681-29	3.511-12	6.3747-9
1.9	4.533-22	2.469-20	7.175-16	2.5901-1	7.2112-2	1.331-27	6.196-11	7.0171-8
2.0	1.767-20	4.083-19	4.310-15	2.5847-1	7.2649-2	3.651-26	7.345-10	5.5015-7
2.1	4.125-19	4.508-18	1.995-14	2.5680-1	7.4318-2	6.174-25	6.3367-9	3.2882-6
2.2	6.290-18	3.556-17	7.432-14	2.5401-1	7.7076-2	6.974-24	4.2161-8	1.5739-5
2.3	6.658-17	2.099-16	2.295-13	2.5009-1	8.0935-2	5.555-23	2.2532-7	6.2430-5
2.4	5.090-16	9.554-16	5.984-13	2.4495-1	8.5947-2	3.231-22	9.9446-7	2.1008-4
2.5	2.876-15	3.409-15	1.332-12	2.3845-1	9.2191-2	1.397-21	3.6871-6	6.0835-4
2.6	1.218-14	9.627-15	2.542-12	2.3045-1	9.9734-2	4.540-21	1.1607-5	1.5297-3
2.7	3.907-14	2.168-14	4.181-12	2.2089-1	1.0858-1	1.118-20	3.1268-5	3.3634-3
2.8	9.662-14	3.945-14	5.972-12	2.0979-1	1.1861-1	2.116-20	7.2774-5	6.5226-3
2.9	1.889-13	5.918-14	7.499-12	1.9737-1	1.2962-1	3.159-20	1.4825-4	1.1289-2
3.0	3.010-13	7.509-14	8.411-12	1.8391-1	1.4131-1	3.832-20	2.6866-4	1.7698-2
3.1	4.040-13	8.274-14	8.569-12	1.6973-1	1.5338-1	3.899-20	4.4104-4	2.5537-2
3.2	4.708-13	8.112-14	8.051-12	1.5514-1	1.6558-1	3.427-20	6.6780-4	3.4450-2
3.3	4.879-13	7.210-14	7.058-12	1.4037-1	1.7771-1	2.658-20	9.4778-4	4.4045-2
3.4	4.577-13	5.887-14	5.818-12	1.2561-1	1.8964-1	1.846-20	1.2782-3	5.3978-2
3.5	3.930-13	4.447-14	4.527-12	1.1098-1	2.0126-1	1.155-20	1.6562-3	6.3974-2
3.6	3.104-13	3.114-14	3.323-12	9.6590-2	2.1249-1	6.514-21	2.0802-3	7.3831-2
3.7	2.253-13	2.012-14	2.292-12	8.2533-2	2.2327-1	3.280-21	2.5506-3	8.3406-2
3.8	1.491-13	1.187-14	1.470-12	6.8894-2	2.3350-1	1.449-21	3.0707-3	9.2593-2
3.9	8.853-14	6.271-15	8.626-13	5.5770-2	2.4311-1	5.440-22	3.6479-3	1.0131-1
4.0	4.577-14	2.868-15	4.497-13	4.3283-2	2.5193-1	1.649-22	4.2956-3	1.0949-1

Specie Mole Fraction as a function of O/F Ratio at a Chamber Pressure of 170 psig

170.0	C	CH	CN	CO	CO2	C2	NO	OH
1.5	4.654-31	2.918-27	2.729-20	2.4964-1	7.9929-2	9.051-36	6.436-17	6.561-13
1.6	9.648-29	1.792-25	3.727-19	2.5301-1	7.8002-2	1.136-33	2.270-15	1.335-11
1.7	3.798-26	1.817-23	7.139-18	2.5632-1	7.4803-2	2.662-31	1.182-13	3.707-10
1.8	6.159-24	9.198-22	8.794-17	2.5833-1	7.2799-2	2.759-29	3.456-12	6.2759-9
1.9	4.521-22	2.501-20	7.273-16	2.5901-1	7.2118-2	1.368-27	6.095-11	6.9045-8
2.0	1.761-20	4.131-19	4.366-15	2.5846-1	7.2658-2	3.746-26	7.220-10	5.4097-7
2.1	4.103-19	4.556-18	2.019-14	2.5678-1	7.4330-2	6.327-25	6.2234-9	3.2312-6
2.2	6.248-18	3.590-17	7.517-14	2.5400-1	7.7090-2	7.137-24	4.1376-8	1.5456-5
2.3	6.608-17	2.117-16	2.320-13	2.5008-1	8.0950-2	5.680-23	2.2103-7	6.1289-5
2.4	5.052-16	9.637-16	6.049-13	2.4494-1	8.5962-2	3.303-22	9.7553-7	2.0624-4
2.5	2.857-15	3.442-15	1.347-12	2.3844-1	9.2205-2	1.430-21	3.6192-6	5.9756-4
2.6	1.212-14	9.736-15	2.574-12	2.3046-1	9.9746-2	4.656-21	1.1408-5	1.5043-3
2.7	3.902-14	2.198-14	4.240-12	2.2090-1	1.0859-1	1.149-20	3.0791-5	3.3128-3
2.8	9.685-14	4.011-14	6.068-12	2.0982-1	1.1863-1	2.184-20	7.1835-5	6.4369-3
2.9	1.900-13	6.035-14	7.634-12	1.9740-1	1.2964-1	3.271-20	1.4670-4	1.1164-2
3.0	3.039-13	7.677-14	8.578-12	1.8393-1	1.4135-1	3.980-20	2.6650-4	1.7536-2
3.1	4.090-13	8.476-14	8.750-12	1.6974-1	1.5345-1	4.061-20	4.3843-4	2.5346-2
3.2	4.777-13	8.323-14	8.229-12	1.5513-1	1.6567-1	3.575-20	6.6508-4	3.4240-2
3.3	4.959-13	7.406-14	7.218-12	1.4034-1	1.7783-1	2.776-20	9.4539-4	4.3829-2
3.4	4.656-13	6.050-14	5.952-12	1.2556-1	1.8978-1	1.928-20	1.2766-3	5.3765-2
3.5	4.000-13	4.571-14	4.630-12	1.1090-1	2.0143-1	1.207-20	1.6559-3	6.3771-2
3.6	3.160-13	3.199-14	3.398-12	9.6493-2	2.1269-1	6.798-21	2.0816-3	7.3645-2
3.7	2.293-13	2.066-14	2.342-12	8.2415-2	2.2349-1	3.418-21	2.5542-3	8.3239-2
3.8	1.516-13	1.217-14	1.500-12	6.8756-2	2.3375-1	1.507-21	3.0770-3	9.2448-2
3.9	8.986-14	6.417-15	8.787-13	5.5615-2	2.4337-1	5.640-22	3.6576-3	1.0119-1
4.0	4.634-14	2.926-15	4.569-13	4.3117-2	2.5220-1	1.702-22	4.3092-3	1.0940-1

Vita

Lester Langford was born in Houma, LA on May 25, 1959, the son of Katherin Fowler Langford and W. Worth Langford. He currently resides in Slidell, LA, with his wife, Megan, and his daughter, Katherin. Starting university in 1996, he received his B.S. in Electrical Engineering from the University of New Orleans in 2003. He entered the Graduate Program at the University of New Orleans in 2004. He has been employed at Stennis Space Center in Mississippi since 1991, where he has been involved in the development and application of spectroscopic techniques to the field of rocket engine ground testing.

Permanent Address: 501 Timberlane Drive
 Slidell, Louisiana, 70458

This thesis was typed by the author.